Available online at www.sciencedirect.com
ScienceDirect
International Journal of Multiphase Flow 33 (2007) 182–206
International Journal of Multiphase Flow
www.elsevier.com/locate/ijmulflow

Low-Reynolds-number motion of a deformable drop between two parallel plane walls

Andrew J. Griggs, Alexander Z. Zinchenko *, Robert H. Davis *

Department of Chemical and Biological Engineering, University of Colorado, Boulder, CO 80309-0424, USA

Received 2 January 2006; received in revised form 20 June 2006

Abstract

The motion of a three-dimensional deformable drop between two parallel plane walls in a low-Reynolds-number Poiseuille flow is examined using a boundary-integral algorithm that employs the Green's function for the domain between two infinite plane walls, which incorporates the wall effects without discretization of the walls. We have developed an economical calculation scheme that allows long-time dynamical simulations, so that both transient and steady-state shapes and velocities are obtained. Results are presented for neutrally buoyant drops having various viscosity, size, deformability, and channel position. For nearly spherical drops, the decrease in translational velocity relative to the undisturbed fluid velocity at the drop center increases with drop size, proximity of the drop to one or both walls, and drop-to-medium viscosity ratio. When deformable drops are initially placed off the centerline of flow, lateral migration towards the channel center is observed, where the drops obtain steady shapes and translational velocities for subcritical capillary numbers. With increasing capillary number, the drops become more deformed and have larger steady velocities due to larger drop-to-wall clearances. Non-monotonic behavior for the lateral migration velocities with increasing viscosity ratio is observed. Simulation results for large drops with non-deformed spherical diameters exceeding the channel height are also presented.

Keywords: Drops; Bubbles; Channel; Boundary-integral; Stokes flow

1. Introduction

Droplet motion in confined geometries, aside from being of fundamental interest, is relevant to several application areas, ranging from multiphase fluid flow through porous media to the transport of cells or other biological media in capillaries and microfluidic devices. In the present work, the behavior of a single deformable drop in a Poiseuille flow between two infinite parallel plane walls is examined by numerical simulation, focusing primarily on cases when the drop size is comparable to the channel height, i.e. when the bounding walls affect the drop shape and mobility.

* Corresponding authors. Tel.: +1 303 492 7314; fax: +1 303 492 4341.
E-mail addresses: alexander.zinchenko@colorado.edu (A.Z. Zinchenko), robert.davis@colorado.edu (R.H. Davis).

0301-9322/$ - see front matter
doi:10.1016/j.ijmultiphaseflow.2006.06.012

The motion of spherical or nearly spherical drops in a channel consisting of two parallel walls has received attention by a variety of exact and approximate methods. The parallel motion of a nearly spherical drop between two channel walls in a quiescent fluid was considered by Shapira and Haber (1988) using the method of reflections. Approximate solutions for the hydrodynamic drag force exerted on the droplet were obtained, which are accurate when the drop-to-wall spacing is not small. More recently, Chen and Keh (2001) utilized a boundary-collocation technique to examine the parallel motion of spherical drops moving near one plane wall and between two parallel plates as a function of drop size and viscosity ratio. The solutions of Chen and Keh (2001) agree well with a previous study on the motion of rigid spheres (Ganatos et al., 1980) when the drop-to-medium viscosity ratio tends to infinity. The motion of rigid particles in Stokes flow between two planar walls has also been studied (Staben et al., 2003), where a boundary-integral method was used to find the translational and rotational velocities of spherical and ellipsoidal particles, as functions of particle size and location in the channel.

In comparison to numerical investigations involving rigid particles, there are two primary factors arising for deformable drops that introduce enriched physical phenomena at low-Reynolds number. First, one must consider the dynamically coupled flows exterior and interior to the drop interface. Second, the viscous stresses exerted on the drops by the flow give rise to deformations. In contrast to spherical drops and particles, a neutrally buoyant drop in fully developed channel flow is capable of crossing streamlines, as a consequence of drop deformation. Under such conditions, the drops can obtain a variety of transient non-spherical shapes, requiring dynamical simulations and an accompanying increased computational demand compared to non-deformable drops or rigid particles.

The lateral migration of two-dimensional drops in a channel consisting of two parallel plane walls has been studied numerically for finite Reynolds number (Mortazavi and Tryggvasson, 2000), with the full Navier–Stokes equations solved by a second-order projection method, using a finite-difference/front-tracking approach to examine dynamical drop behavior, primarily as a function of the Reynolds number. Although the study was focused towards higher Reynolds numbers and smaller relative drop sizes and deformations than those in the present work, some small inertia ($Re = 0.25$) cases for neutrally buoyant drops were considered. Of particular interest, when deformable drops with diameter 1/4 of the channel height were initially placed off the centerline of flow, movement towards the centerline for a low-viscosity drop was reported, while migration away from the centerline was observed for a drop with viscosity matching the external fluid. The motion of a two-dimensional bubble rising in an inclined channel, with and without insoluble surfactant, has also received attention by a boundary-integral method (DeBisschop et al., 2002).

Also related to the problem at hand is the motion of deformable drops through cylindrical tubes, which has received considerable attention and is motivated by several applications in the field of biomechanics. For example, the motion of red blood cells through veins or capillaries, as well as the fate of gas bubbles in the blood stream, is of significant biological and clinical interest. Olbricht and Kung (1992) have experimentally studied the motion of drops in straight tubes for an extensive range of parameters. The axisymmetric motion of deformable drops in pressure-driven flow has been considered by Martinez and Udell (1990). The deformation of axisymmetric drops and bubbles moving through straight tubes and constrictions under pressure-driven flow have been studied by Tsai and Miksis (1994) as a function of capillary number. Using a combination of lubrication theory for the thin film between the drop and the tube wall and a two-dimensional boundary-integral representation for the internal flow, Hodges et al. (2004) recently considered the motion of a semi-infinite drop moving through a cylindrical tube. Such approaches are not a replacement for the numerical simulations in our work, since they are valid for over a limited range of parameters (e.g. very small-drop-to-wall clearances and capillary numbers) and have only logarithmic accuracy. Coulliette and Pozrikidis (1998) considered the transient motion of a periodic file of three-dimensional drops in a cylindrical tube by numerical simulation for subcritical capillary numbers. In their study, the drop-to-medium viscosity and density ratios were fixed at unity and the surface tension was assumed constant. The principal objective of then analysis was to extend previous two-dimensional and axisymmetric studies of drop motion by examining the dynamics of droplet migration, when the drops are initially placed off the centerline of flow. Assuming the capillary number is sufficiently large, the drops begin to deform from their initially spherical shape, migrate towards the centerline of flow, and then approach a steady shape after a preliminary stage of rapid deformation. The results given by Coulliette and Pozrikidis (1998) provide some

of the first three-dimensional computed drop shapes for drop motion in a confined container at low-Reynolds number.

While the numerous studies discussed above constitute considerable progress towards understanding the low-Reynolds-number motion of drops in tubes and channels, there still remain some important unresolved issues and computational challenges. In particular, there is a need for a three-dimensional systematic study of the motion of a deformable drop between two parallel walls in the Stokes flow regime. Thus, the primary aim of the current work is to develop and employ an efficient and accurate three-dimensional boundary-integral method for the motion of a neutrally buoyant deformable drop between two parallel plane walls, encompassing various drop sizes, capillary numbers, positions within the channel, and drop-to-medium viscosity ratios. Previous works on the low-Reynolds-number motion of deformable drops in an unbounded medium have provided many of the necessary computational advancements (Zinchenko et al., 1997, 1999; Zinchenko and Davis, 2000). In combination with the work by Staben et al. (2003) on rigid particles, these contributions offer the framework for the study of a deformable droplet confined between two parallel plane walls. Central to the numerical formulation is a newly improved, efficient version of the Green's function for the domain between two parallel walls, originally constructed using repeated reflections by Liron and Mochon (1976) and later adapted to boundary-integral calculations (Staben et al., 2003). The boundary-integral formulation for the problem is given in Section 2, essential details regarding our numerical procedures are given in Section 3, and the substantial improvements to the calculation of the most demanding portion of the boundary-integral equation are discussed in the Appendix A. Numerical results are given in Section 4, where we examine both dynamic measures, such as drop migration and deformation modes, and steady-state quantities, such as equilibrium drop locations within the channel, shapes, and translational velocities. The presented three-dimensional results, which have physically meaningful differences than those from previous two-dimensional studies, show the complicated relationship between the drop mobility and non-axisymmetric drop shapes. Long-time calculations involving large drops comparable to the channel dimensions are studied, including difficult cases when the non-deformed spherical diameter of the drop exceeds the channel height.

2. Boundary-integral formulation

We consider a deformable drop freely suspended in a Poiseuille flow between two parallel plane walls at low-Reynolds number. Both the drop and external suspending fluid are assumed Newtonian, devoid of surfactants, and have viscosities μ_d and μ_e, respectively, with matching densities ($\rho_d = \rho_e$). For any point on the drop surface, S, the interfacial velocity, $\mathbf{u}(\mathbf{y})$, satisfies the boundary-integral equation for a deformable interface (Rallison and Acrivos, 1978)

$$u^l(\mathbf{y}) = 2\kappa \int_S \mathbf{u}(\mathbf{x}) \cdot \boldsymbol{\tau}^l(\mathbf{x};\mathbf{y}) \cdot \mathbf{n}(\mathbf{x}) \mathrm{d}S_{\mathbf{x}} + F^l(\mathbf{y}), \tag{1}$$

$$F^l(\mathbf{y}) = \frac{2}{(\eta+1)} \left(\frac{1}{\mu_e} \int_S f(\mathbf{x}) \mathbf{n}(\mathbf{x}) \cdot \mathbf{G}^l(\mathbf{x};\mathbf{y}) \mathrm{d}S_{\mathbf{x}} + u^l_\infty \right), \tag{2}$$

where $\mathbf{G}^l(\mathbf{x};\mathbf{y})$ is the Green's function for the domain between two parallel walls, i.e. the Stokes velocity generated at $\mathbf{x}$ by the unit point force applied to $\mathbf{y}$ along the Cartesian coordinate axis ($l = 1,2,3$), for unit viscosity and no slip at the walls. Here, the stress tensor corresponding to the fundamental solution is $\boldsymbol{\tau}^l(\mathbf{x};\mathbf{y}) = \{\tau^l_{ij}(\mathbf{x};\mathbf{y})\}$, $\mathbf{n}(\mathbf{x})$ is the outward-pointing unit normal vector, the drop-to-medium viscosity ratio is $\eta = \mu_d/\mu_e$, and $\kappa = (\eta-1)/(\eta+1)$. Finally, $f(\mathbf{x}) = 2\sigma k(\mathbf{x})$, so that $f(\mathbf{x})\mathbf{n}(\mathbf{x})$ is the stress jump across the interface due to the constant surface tension, σ, where $k(\mathbf{x}) = \frac{1}{2}(k_1 + k_2)$ is the local mean curvature. The right Cartesian coordinate system x_1, x_2, x_3 is chosen such that the plane $x_3 = 0$ serves as the lower wall and the direction of the flow is along the x_2 axis (Fig. 1). The parabolic flow far from the drop is

$$\mathbf{u}_\infty = \frac{4U_c x_3}{H}\left(1 - \frac{x_3}{H}\right)\mathbf{e}_2, \tag{3}$$

where H is the channel height and U_c is the Poiseuille flow velocity in the channel midplane, $x_3 = H/2$. The Reynolds number, $Re = \rho_e U_c H/\mu_e$, is assumed to be small compared to unity.

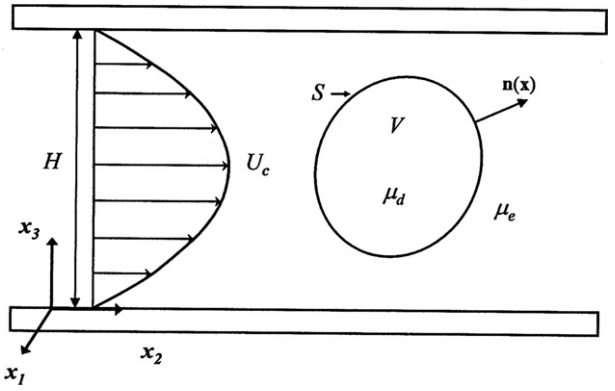

Fig. 1. Geometry and coordinate system for the motion of a drop between two parallel plane walls under Poiseuille flow.

The marginal eigenvalues ($\kappa = \pm 1$) of (1) can be purged through Wielandt deflation (Kim and Karrila, 1991; Pozrikidis, 1992), resulting in faster convergence of iterative solutions for $\eta \ll 1$ or $\eta \gg 1$. The deflated form of the boundary-integral equation is

$$w_l(\mathbf{y}) = \kappa\left[2\int_S \mathbf{w}(\mathbf{x})\cdot\boldsymbol{\tau}^l(\mathbf{x};\mathbf{y})\cdot\mathbf{n}(\mathbf{x})\mathrm{d}S_{\mathbf{x}} - w'_l(\mathbf{y}) + \frac{n_l(\mathbf{y})}{S}\int_S \mathbf{w}(\mathbf{x})\cdot\mathbf{n}(\mathbf{x})\mathrm{d}S_{\mathbf{x}}\right] + F^l(\mathbf{y}) \tag{4}$$

for $\mathbf{w} = \mathbf{u} - \kappa\mathbf{u}'$, where the prime denotes the projection of the vector field on the space of rigid body motions, and

$$\mathbf{u} = \mathbf{w} + \frac{\kappa}{1-\kappa}\mathbf{w}'. \tag{5}$$

Following singularity and near-singularity subtraction (see below), (4) becomes suitable for efficient numerical solutions.

The field $\mathbf{w}'(\mathbf{y})$ can be calculated without Gram–Schmidt orthogonalization, simply as (Zinchenko et al., 1997)

$$\mathbf{w}'(\mathbf{y}) = A_i\mathbf{e}_i + B_i\mathbf{e}_i \times \hat{\mathbf{x}}, \tag{6}$$

where $\hat{\mathbf{x}} = \mathbf{x} - \mathbf{x}_c$ and

$$\mathbf{x}_c = \frac{1}{S}\int_S \mathbf{x}\,\mathrm{d}S \tag{7}$$

is the surface centroid,

$$A_i = \frac{1}{S}\int_S w_i(\mathbf{x})\mathrm{d}S \quad (i = 1,2,3), \tag{8}$$

and the coefficients B_i $(i = 1,2,3)$ are calculated from the solution of a 3×3 system

$$D_{ij}B_j = \int_S \mathbf{w}(\mathbf{x})\cdot[\mathbf{e}_i \times \hat{\mathbf{x}}]\mathrm{d}S, \tag{9}$$

where D_{ij} is a positive-definite matrix

$$D_{ij} = \int_S [\delta_{ij}\hat{\mathbf{x}}^2 - \hat{x}_i\hat{x}_j]\mathrm{d}S. \tag{10}$$

3. Numerical method

Explicit expressions for the Green's function components for the domain between two parallel walls, G^l_j, and the corresponding pressures, p^l, have been derived by Liron and Mochon (1976) in terms of infinite

Fourier–Bessel integrals, which, unfortunately, are extremely cumbersome and impractical for direct use in dynamic simulations. The starting point of our approach is to represent the Green's function as the sum of four contributions: $\mathbf{G}^l = \mathbf{G}^l_0 + \mathbf{G}^l_{\mathrm{LW}} + \mathbf{G}^l_{\mathrm{UW}} + \hat{\mathbf{G}}^l$, for the free-space part, lower-wall and upper-wall corrections, and the two-wall interaction term, respectively. The indices LW and UW denote lower-wall and upper-wall corrections, so that, for example, $\mathbf{G}^l_0 + \mathbf{G}^l_{\mathrm{LW}}$ is the Green's function for the whole half-space $x_3 > 0$, derived by Blake (1971) and summarized by Pozrikidis (1992). Advantages of using the Green's function for the confined domain, in combination with boundary-integral methods, include that discretization of the bounding walls is not required (instead only the drop surface must be discretized) and the resulting second-kind integral equation has spectral properties suitable for iterative solution by successive substitutions (Kim and Karrila, 1991; Pozrikidis, 1992).

The free-space Green's function originates from the fundamental solution for the point-force velocity in an unbounded fluid,

$$(G^l_i)_0(\mathbf{x};\mathbf{y}) = -\frac{1}{8\pi}\left[\frac{\delta_{il}}{r} + \frac{r_i r_l}{r^3}\right], \tag{11}$$

with $\mathbf{r} = \mathbf{x} - \mathbf{y}$ and $r = \|\mathbf{r}\|$. Singular behavior in the free-space portion, as $\mathbf{x} \to \mathbf{y}$, is handled by standard singularity subtraction:

$$\int_S f(\mathbf{x})\mathbf{n}(\mathbf{x}) \cdot \mathbf{G}^l_0(\mathbf{x};\mathbf{y})\mathrm{d}S_{\mathbf{x}} = \int_S [f(\mathbf{x}) - f(\mathbf{y})]\mathbf{n}(\mathbf{x}) \cdot \mathbf{G}^l_0(\mathbf{x};\mathbf{y})\mathrm{d}S_{\mathbf{x}}, \quad \mathbf{y} \in S. \tag{12}$$

A similar desingularization is made for the free-space contribution to the double layer using the identity $\int_S \boldsymbol{\tau}^l_0(\mathbf{x};\mathbf{y}) \cdot \mathbf{n}(\mathbf{x})\mathrm{d}S_{\mathbf{x}} = \frac{1}{2}\mathbf{e}_l$ for $\mathbf{y} \in S$, yielding

$$\int_S \mathbf{w}(\mathbf{x}) \cdot \boldsymbol{\tau}^l_0(\mathbf{x};\mathbf{y}) \cdot \mathbf{n}(\mathbf{x})\mathrm{d}S_{\mathbf{x}} = \frac{1}{2}w_l(\mathbf{y}) + \frac{3}{4\pi}\int_S \frac{[\mathbf{r} \cdot \mathbf{n}(\mathbf{x})][\mathbf{r} \cdot (\mathbf{w}(\mathbf{x}) - \mathbf{w}(\mathbf{y}))]r_l}{r^5}\mathrm{d}S_{\mathbf{x}}. \tag{13}$$

The lower-wall correction to the fundamental solution is

$$(\mathbf{G}^l_i)_{\mathrm{LW}}(\mathbf{x};\mathbf{y}) = -\frac{1}{8\pi}\left(\left[-\frac{\delta_{il}}{R} - \frac{R_i R_l}{R^3}\right] + m\left\{2y_3(y_3 - R_3)\left[\frac{\delta_{il}}{R^3} - 3\frac{R_i R_l}{R^5}\right] - 2y_3\left[\frac{\delta_{l3}R_i - \delta_{i3}R_l}{R^3}\right]\right\}\right), \tag{14}$$

where $\mathbf{R} = \mathbf{x} - \mathbf{y}^*_{\mathrm{LW}}$, $\mathbf{y}^*_{\mathrm{LW}}$ is the mirror image of the point $\mathbf{y}$ with respect to the lower wall, $R = \|\mathbf{R}\|$, and $m = \pm 1$, with the plus sign for $l = 1, 2$ and minus for $l = 3$. The upper-wall correction can be obtained by replacing y_3 with $(y_3 - H)$ and $\mathbf{y}^*_{\mathrm{LW}}$ with $\mathbf{y}^*_{\mathrm{UW}}$ in (14). The lower- and upper-wall corrections possess singularities when $\mathbf{x} = \mathbf{y}^*_{\mathrm{LW}}$ and $\mathbf{x} = \mathbf{y}^*_{\mathrm{UW}}$, respectively. To significantly improve the accuracy of calculations when the drop is close to either or both walls, integrations involving the lower- and upper-wall corrections are subject to near-singularity subtraction (Staben et al., 2003)

$$\int_S f(\mathbf{x})\mathbf{n}(\mathbf{x}) \cdot \mathbf{G}^l_{\mathrm{LW}}(\mathbf{x};\mathbf{y})\mathrm{d}S_{\mathbf{x}} = \int_S [f(\mathbf{x}) - f(\mathbf{x}^0_{\mathrm{LW}})]\mathbf{n}(\mathbf{x}) \cdot \mathbf{G}^l_{\mathrm{LW}}(\mathbf{x};\mathbf{y})\mathrm{d}S_{\mathbf{x}} \quad \text{for } \mathbf{y} \in S, \tag{15}$$

where $\mathbf{x}^0_{\mathrm{LW}}$ is the mesh point on S closest to the mirror image of point $\mathbf{y}$ with respect to the lower wall; for the upper-wall correction, $\mathbf{x}^0_{\mathrm{UW}}$, has a similar meaning, and the analog of (15) is used.

Since $\tau^l_{\mathrm{LW}}(\mathbf{x};\mathbf{y})$ and $\tau^l_{\mathrm{UW}}(\mathbf{x};\mathbf{y})$ are divergence-free tensors for $\mathbf{x}$ between the walls, the double-layer integrals are transformed as

$$\int_S \mathbf{w}(\mathbf{x}) \cdot \boldsymbol{\tau}^l_{\mathrm{LW}}(\mathbf{x};\mathbf{y}) \cdot \mathbf{n}(\mathbf{x})\mathrm{d}S_{\mathbf{x}} = \int_S [\mathbf{w}(\mathbf{x}) - \mathbf{w}(\mathbf{x}^0_{\mathrm{LW}})] \cdot \boldsymbol{\tau}^l_{\mathrm{LW}}(\mathbf{x};\mathbf{y}) \cdot \mathbf{n}(\mathbf{x})\mathrm{d}S_{\mathbf{x}}, \tag{16}$$

$$\int_S \mathbf{w}(\mathbf{x}) \cdot \boldsymbol{\tau}^l_{\mathrm{UW}}(\mathbf{x};\mathbf{y}) \cdot \mathbf{n}(\mathbf{x})\mathrm{d}S_{\mathbf{x}} = \int_S [\mathbf{w}(\mathbf{x}) - \mathbf{w}(\mathbf{x}^0_{\mathrm{UW}})] \cdot \boldsymbol{\tau}^l_{\mathrm{UW}}(\mathbf{x};\mathbf{y}) \cdot \mathbf{n}(\mathbf{x})\mathrm{d}S_{\mathbf{x}}. \tag{17}$$

The expressions for the wall-correction integrands involving the stress tensor are

$$\begin{aligned}\Delta\mathbf{w} \cdot \boldsymbol{\tau}^l_{\mathrm{LW}}(\mathbf{x};\mathbf{y}) \cdot \mathbf{n}(\mathbf{x}) = &-\frac{3}{4\pi}\frac{(\mathbf{R} \cdot \mathbf{n})(\mathbf{R} \cdot \Delta\mathbf{w})R_l}{R^5} - \frac{3}{2\pi}\frac{y_3 m}{R^5}\left[\left(\frac{5(y_3 - R_3)(\mathbf{R} \cdot \mathbf{n})(\mathbf{R} \cdot \Delta\mathbf{w})}{R^2} - y_3(\Delta\mathbf{w} \cdot \mathbf{n})\right)R_l\right. \\ &\left. + (R_3 - y_3)[(\mathbf{R} \cdot \mathbf{n})\Delta w_l + (\mathbf{R} \cdot \Delta\mathbf{w})n_l] + (\mathbf{R} \cdot \mathbf{n})(\mathbf{R} \cdot \Delta\mathbf{w})\delta_{l3}\right],\end{aligned} \tag{18}$$

where $\Delta\mathbf{w} = \mathbf{w}(\mathbf{x}) - \mathbf{w}(\mathbf{x}^0_{\mathrm{LW}})$, $\mathbf{n} = \mathbf{n}(\mathbf{x})$, and $\mathbf{R} = \mathbf{x} - \mathbf{y}^*_{\mathrm{LW}}$ with a similar expression for the upper-wall integrand if $\Delta\mathbf{w} = \mathbf{w}(\mathbf{x}) - \mathbf{w}(\mathbf{x}^0_{\mathrm{UW}})$, $\mathbf{R} = \mathbf{x} - \mathbf{y}^*_{\mathrm{UW}}$, and y_3 in (18) is replaced by $y_3 - H$.

The two-wall interaction term, $\widehat{\mathbf{G}}^I$, accounts for the presence of both walls simultaneously and can be viewed as a result of repeated reflections taken to satisfy the no-slip condition at the walls (Bhattacharya and Blawzdziewicz, 2002), and its calculation is the most cumbersome and computationally expensive portion of the simulation. The contribution, $\widehat{\mathbf{G}}^I$, is a smooth function of $\mathbf{x}$ and $\mathbf{y}$ up to the walls and is not singular at $\mathbf{x} = \mathbf{y}$, nor when $\mathbf{x}$ and $\mathbf{y}$ are both close to either wall. A previous study on rigid spheres represented this interaction term as a collection of regularized Fourier–Bessel integrals (Staben et al., 2003), which eliminated the poorly convergent behavior of the original solution (Liron and Mochon, 1976) for the extreme cases listed above. However, direct evaluation of the regularized integrals in the dynamical simulations for deformable drops would still be prohibitively expensive. An alternative to direct calculation might be to pre-tabulate and then interpolate the smooth tensor, $\widehat{\mathbf{G}}^I(\mathbf{x};\mathbf{y})$, from tables, but this approach is still much too computationally demanding for long-time dynamic simulations, given the complex structure of $\widehat{\mathbf{G}}^I(\mathbf{x};\mathbf{y})$ (Staben et al., 2003) and the large number of interpolations required. We have instead devised a more economical scheme to calculate $\widehat{\mathbf{G}}^I(\mathbf{x};\mathbf{y})$ based on Taylor expansions about the drop center, $\mathbf{x}_c$, as described in the Appendix A. The numerical accuracy of the Taylor expansions was assessed by comparing to direct calculations of the regularized Fourier–Bessel integrals. Compared to small drops, a large drop that is close to both walls requires a greater number of retained terms in the expansions to obtain convergence.

For our simulations, the drop was typically started from a spherical shape. Several surface discretization schemes were used to generate unstructured, highly uniform triangulations of a spherical surface from a regular polyhedron, followed by a series of refinements. These schemes yield discretizations with $N_\triangle = 20\times 4^n$ or 60×4^n ($n = 0, 1, 2, \ldots$) triangular elements, plus additional possibilities of $N_\triangle = 720$, 1500, 2160, 2880, and 6000 (Zinchenko et al., 1997; Staben et al., 2003). Each triangulation has $N_\triangle/2 + 2$ triangle vertices with a maximum-to-minimum mesh edge ratio between 1.19 and 1.22. In cases where the drop started from an ellipsoidal shape, triangulations were performed for a unit sphere and then transformed by simple stretching.

Eq. (4) is approximated as a linear system for unknowns, $\mathbf{w}(\mathbf{y}_n)$, at the triangle vertices on the drop surface, which serve as the only collocation points. For any smooth function $\varphi(\mathbf{x})$ on S, a simple surface trapezoidal rule is used with reassignment of the triangle contributions to the vertices (Rallison, 1981):

$$\int_S \varphi(\mathbf{x})\mathrm{d}S \approx \sum_{\mathbf{x}_n} \varphi(\mathbf{x}_n)\Delta S_n, \tag{19}$$

$$\Delta S_n = \frac{1}{3}\Delta S, \tag{20}$$

where the summation in (20) is taken over all flat triangle areas ΔS with vertex $\mathbf{x}_n$. For non-matching viscosities, the velocity is obtained by solving (4) using simple iterations. When $\eta = 1$, only (2) requires calculation and the iterative procedure can be bypassed.

For the curvature and normal-vector calculations, the best-paraboloid method is used (Zinchenko et al., 1997, 1999). The standard second-order Runge–Kutta method is used to update the shape and location of the drop interface. To avoid a familiar difficulty with mesh degradation in dynamical simulations, "passive" mesh stabilization techniques are employed to maintain the quality of triangulation as time proceeds. The essence of this procedure is to construct an additional global tangential field on the drop surface from the solution of some variational problem. These additional node velocities act to minimize, in some sense, the "kinetic energy" of the disordered mesh motion. In the simulations of relatively compact drop shapes, a simple approach to mesh preservation (Zinchenko et al., 1997) that seeks to minimize the average rate of change of the distance between neighboring nodes is sufficient. For larger deformations, a more complicated form of the minimizing function that includes curvature adaptation is used, as described by Eqs. (5.3)–(5.6) of Zinchenko et al. (1999). To consider even larger deformations, including those with supercritical capillary numbers where the drops continually deform and are expected to eventually break, a curvatureless form of the boundary integrals (Zinchenko et al., 1999), or mesh restructuring into compact elements (Cristini et al., 1998, 2001), would be required. However, these additional possibilities were not explored, since we examine subcritical deformations in this work.

4. Results and discussion

The dimensionless parameters governing the motion of a neutrally buoyant drop or bubble between two parallel walls are the ratio of drop size to the channel height, drop-to-medium viscosity ratio, and capillary number, in the numerical results presented here, the channel height, H, and the unperturbed fluid velocity at the channel centerline, U_c, have been chosen as the characteristic length and velocity scales for non-dimensionalization, respectively. The capillary number, $Ca = \mu_e U_c/\sigma$, describes the relative magnitude of the viscous to interfacial forces. Drops with reduced non-deformed diameter, $2a/H < 1$, are initially spherical in shape and centered at a prescribed channel position, x_3^c/H. The drop velocity, $\mathbf{U}$, is defined as the fluid velocity averaged over the drop volume and was calculated using Gauss' theorem

$$\mathbf{U} = \frac{1}{V}\int_V \mathbf{u}(\mathbf{x})\mathrm{d}V = \frac{1}{V}\int_S [\mathbf{u}(\mathbf{x})\cdot\mathbf{n}(\mathbf{x})](\mathbf{x}-\mathbf{x}_c)\mathrm{d}S_{\mathbf{x}}. \tag{21}$$

In advancing the solution, we chose a stable timestep, $\Delta t \leqslant bCa\min(\Delta x_{\min}, 0.7\Delta z_{\min})$, where b is a constant, typically limited to be between 1 and 3 to prevent the onset of numerical instabilities, $\Delta x_{\min}$ is the minimum mesh edge, and $\Delta z_{\min}$ is the minimum of all node-to-node distances, $\|\mathbf{x}-\mathbf{y}^*_{\mathrm{UW}}\|$ and $\|\mathbf{x}-\mathbf{y}^*_{\mathrm{LW}}\|$, between the drop interface and its mirror images with respect to the upper and lower walls. The point pairs for which $\mathbf{x}$ is closest to $\mathbf{y}^*_{\mathrm{LW}}$ or $\mathbf{y}^*_{\mathrm{UW}}$ are excluded from the calculation of $\Delta z_{\min}$, since they do not contribute to the boundary integrals after the near-singularity subtraction. This choice of timestep is similar to that employed for two drops in close approach (Zinchenko and Davis, 2005) and ensures adequate stability for calculations of drops in close proximity to the bounding walls.

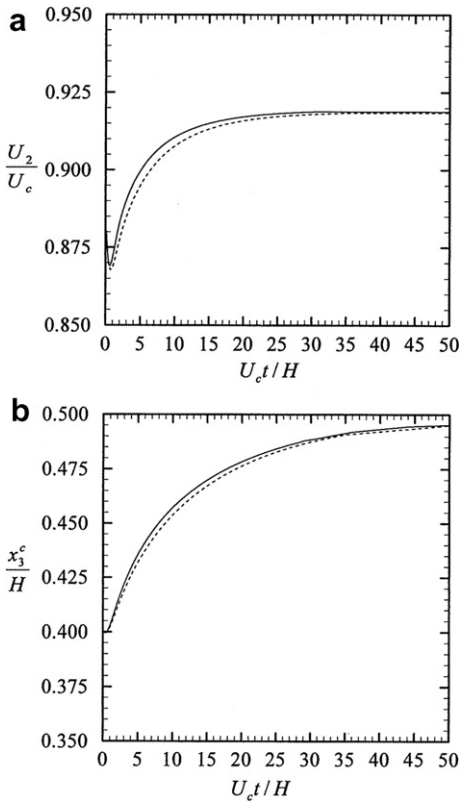

Fig. 2. Comparisons of the solutions with and without the two-wall interaction term for the longitudinal velocity and drop center position with time for $\eta = 1$, $Ca = 0.5$, and $2a/H = 0.6$. The solid line and dashed lines represent the solution with and without the two-wall interaction term, respectively.

4.1. Effect of two-wall interaction term

Although the two-wall interaction term is required to satisfy the boundary conditions at the walls and represents the most burdensome portion of our calculations, we find its contribution to the solution for the steady-state velocity to be relatively small compared to the other contributions. The role of the interaction term in our boundary-integral calculations is illustrated in Fig. 2, where results for the longitudinal velocity and the drop center position are plotted versus time, with and without this term. In Fig. 2, the drop is initially spherical with $2a/H = 0.6$, centered at $x_3^c/H = 0.4$, and $N_\triangle = 3840$ triangular elements were used with $Ca = 0.5$ and $\eta = 1$. Although there is a small but noticeable effect of the interaction term during the initial transient stage of drop deformation and migration, both solutions predict practically the same steady position, $x_3^c/H = 0.5$, and velocity. The simulation times for the results given in Fig. 2 with and without the two-wall interaction term took approximately 252 and 180 min, respectively, using an AMD Athlon XP 2800+ processor under Visual Fortran. The differences in steady-state drop shapes for calculations with and without the interaction term are illustrated in Fig. 3, which shows drop contours as two-dimensional slices in (a) the plane $x_1 = 0$ (side view) and (b) the channel midplane (top view). For these results, the drop was initially positioned at $x_3^c/H = 0.5$ with $2a/H = 0.8$, $Ca = 0.9$, and $\eta = 1$, using $N_\triangle = 6000$. Again, good agreement between the two solutions is obtained for this drop, which is larger and more deformable than the one presented in Fig. 2.

Over a wide range of parameters, the largest discrepancy between the solutions, with and without the two-wall interaction term, for the steady velocities that we observe is less than 1%. From these results for $\eta = 1$, it is clear that the interaction term contributes little to the steady-state quantities of interest. It is also expected that the interaction term makes a negligible contribution to the steady-state results when $\eta \neq 1$, since the integrands in the double-layer integral (4) decay faster than those in the single-layer integral. As shown below for $\eta \gg 1$, the contribution of the two-wall interaction term from the double-layer potential at steady state

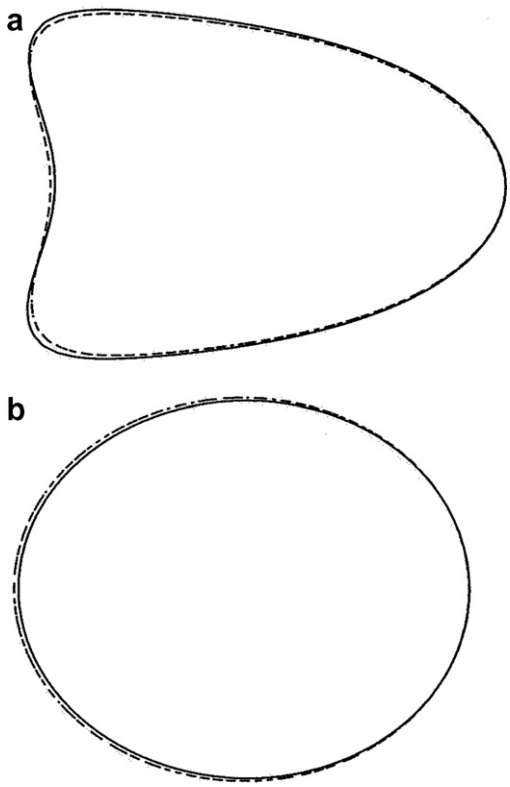

Fig. 3. Comparison of steady drop shapes with $2a/H = 0.8$, $\eta = 1$, and $Ca = 0.9$ for (a) side view and (b) top view. The solid line represents the shape with and the two-wall interaction term the dashed line without.

is indeed negligible and we have chosen to neglect this contribution for $\eta \neq 1$ to not overburden the code at this time. However, the effect of the interaction term may be more important in drop dynamics when the drop is close to both walls. For example, the relative magnitude of the interaction term may be greater when studying the gravity-driven motion of a tightly fitting drop in an inclined channel.

4.2. Velocities of nearly spherical drops

When the capillary number tends to zero, interfacial forces dominate the viscous forces and the drop maintains a spherical shape. As a consequence of the reversibility of the Stokes equations, a neutrally buoyant spherical drop will not migrate across channel streamlines, and so only steady motion parallel to the plane walls results. Computed translational velocities for nearly spherical drops are given in Fig. 4 for a wide range of drop sizes and drop-to-medium viscosity ratios, η, using $N_{\triangle} = 3840$ triangular elements. The velocities of the drops decrease with increasing drop size, proximity to the walls, and drop-to-medium viscosity ratio. Interestingly, the computed velocities are seemingly independent of η for small drops, as they tend to move with the Poiseuille flow rather than lag behind it. Our numerical results for the translational velocity of nearly spherical drops are insensitive to triangulations above $N_{\triangle} = 3840$ for cases when the minimum drop-to-wall spacings are greater than about 1% of the channel height. Additionally, our results for large η ($\sim$15 or greater) and small Ca ($\leqslant$0.05) agree quite well (within about 1%) with previously reported calculations for rigid spheres (Staben et al., 2003), regardless of droplet size or channel location. The observed agreement between our results for $\eta \gg 1$ and those of Staben et al. (2003), who incorporated the two-wall interaction contribution into their double-layer boundary integrals, indicates that the contribution of this term on the double-layer calculation is, indeed, quite small for the steady cases considered here.

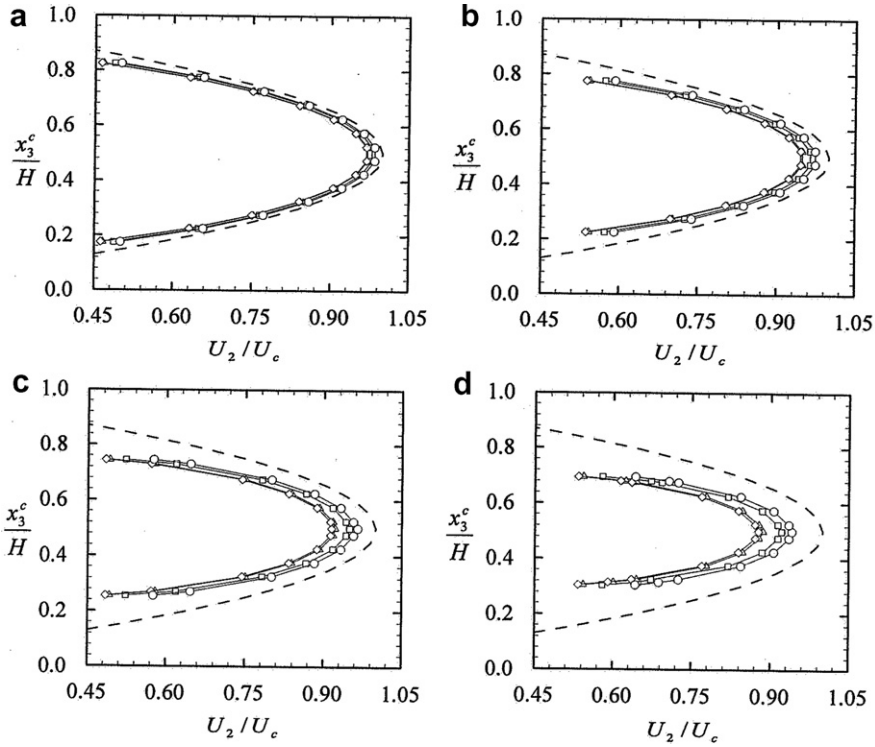

Fig. 4. Simulation results for the dimensionless translational velocities for spherical drops as a function of position of the drop center within the channel, for drops of diameter $2a/H$= (a) 0.3, (b) 0.4, (c) 0.5, (d) 0.6, with viscosity ratios of (○) 0.5, (□) 1.0, (△) 5.0, and (◊) 10 (right to left). The dashed line represents the undisturbed parabolic flow.

4.3. Transient motion of deformable drops

When a deformable drop is placed off the centerplane of flow, migration across channel streamlines occurs, owing to the ability of the drop to adopt non-spherical transient shapes. A similar phenomenon occurs for a deformable drop in shear flow, which migrates away from a nearby wall (Smart and Leighton, 1991; Uijttewaal et al., 1993). In both cases, the drop velocity has components perpendicular and parallel to the walls. Fig. 5 shows computed shapes for the current study at various dimensionless times for the transient migration of a highly deformable drop with $Ca = 1.0$ and $\eta = 1$, for a mesh with $N_{\triangle} = 8640$ triangular elements, which is started from a sphere with diameter $2a/H = 0.6$ positioned at $x_3^c/H = 0.4$. The drop initially elongates in the direction of the Poiseuille flow and migrates away from the lower wall. A tail is evident at intermediate times, which can be attributed to the viscous interaction of the drop with the nearby lower wall. As the drop approaches the channel center, the tail begins to retract and the drop eventually obtains a steady shape that is compact and symmetric about the channel midplane, as shown at time $U_c t/H = 40.61$. This type of dynamic behavior for drop migration is observed for a wide range of viscosity ratios and (subcritical) capillary

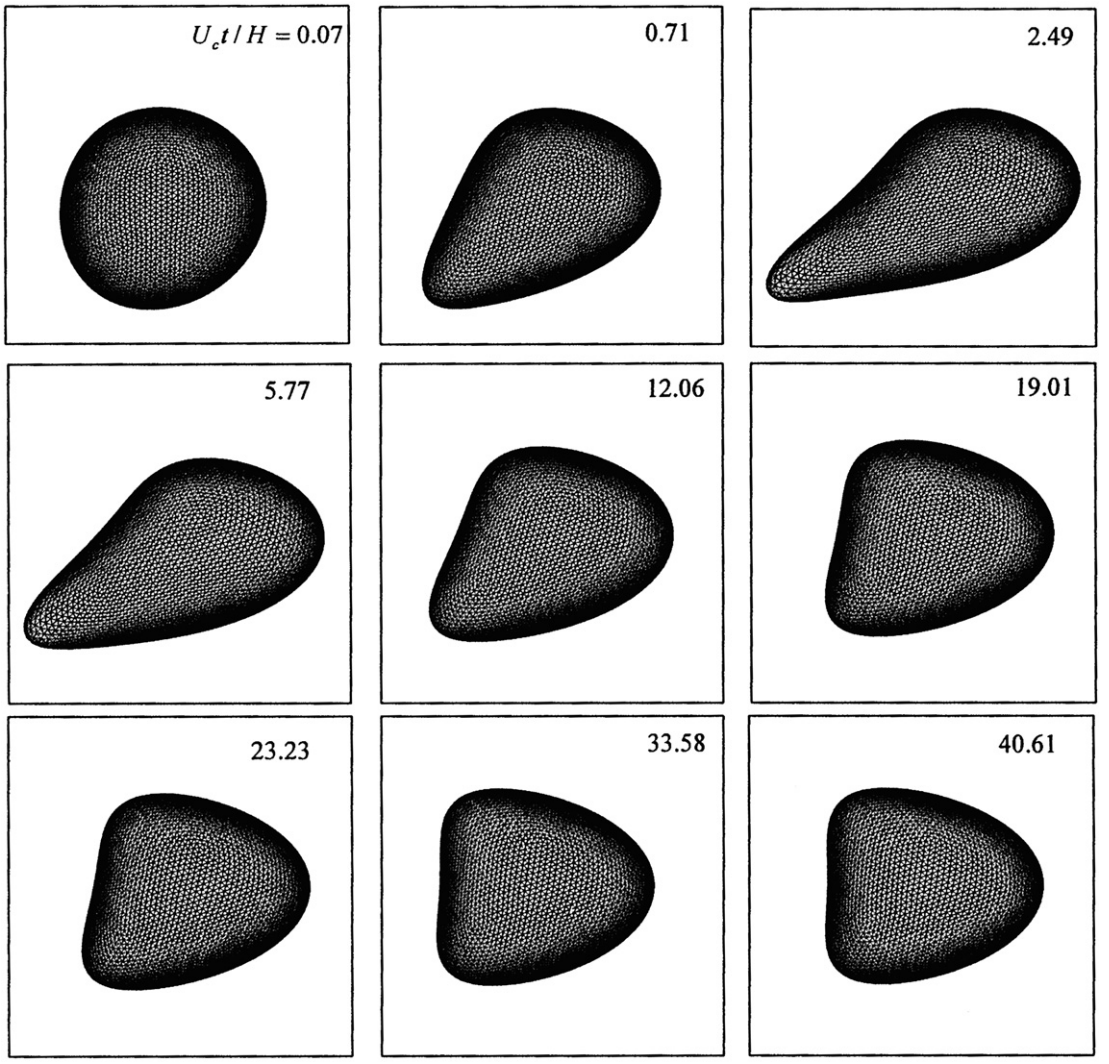

Fig. 5. Snap shots depicting the evolution of a deformable drop initially placed off the centerline of flow at $x_3^c/H = 0.4$, with $\eta = 1.0$, $2a/H = 0.6$, and $Ca = 1.0$ taken at various times. Each box has a height equal to the channel height.

numbers. For example, Fig. 6 gives trends for the longitudinal velocities and the center locations as the drop travels down the channel for $\eta = 1$ and a range of capillary numbers. In the initial phase, a decrease in the longitudinal velocity is observed (Fig. 6a) and can be attributed to the onset of shape distortion, which increases the drop resistance to the flow. Following this initial phase of deformation and migration to the channel center, the translational velocity increases, owing to the streamlined shape adopted by the drops. It is clear from Fig. 6b that the drop migrates increasingly faster towards the channel center with increasing *Ca*, as expected because migration across streamlines only occurs through deformation. Similar behavior has been reported for drop migration away from a single plane wall (Uijttewaal et al., 1993). Fig. 6c shows that the drop deformation increases with increasing capillary number, but this effect is most pronounced during the transient stage.

Over a wide range of initial conditions, we have observed that drops move away from the channel walls, towards the channel center, and obtain a steady position with the drop center in the channel midplane, regardless

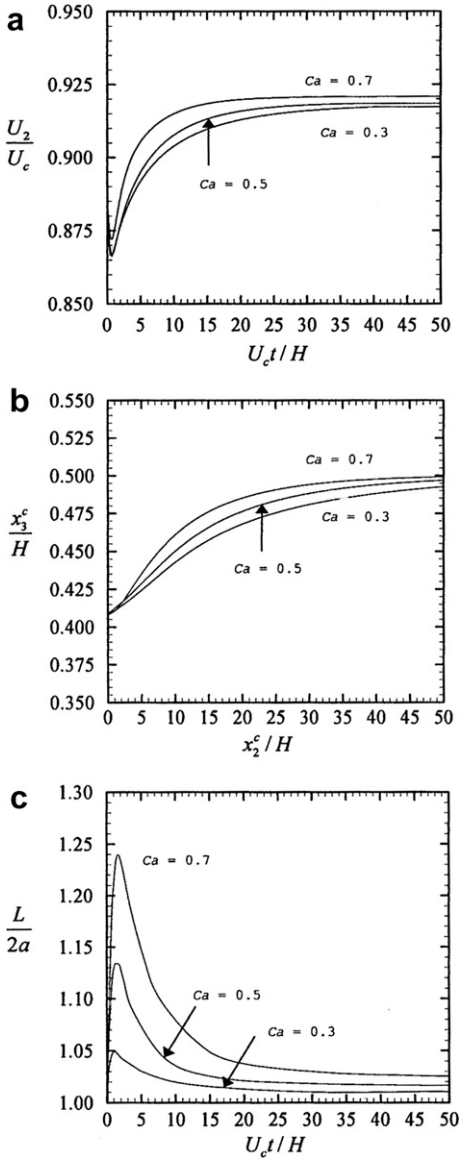

Fig. 6. Simulation results for (a) longitudinal velocities, (b) drop centers, and (c) tip-to-tip drop lengths as functions of time for a drop with for $\eta = 1.0$ and $2a/H = 0.6$ initially located $x_3^c/H = 0.4$.

of the initial placement, size, capillary number, or viscosity ratio. Mortazavi and Tryggvasson (2000) have reported that the direction of drop migration, either towards or away from a bounding wall, depends on the drop-to-medium viscosity ratio, which is apparently a finite-Reynolds-number effect. The tendency of matching-viscosity drops to migrate towards the channel center, rather than towards one wall, is in qualitative agreement with prior results for the initial stages of migration of a periodic file of three-dimensional deformable drops with $\eta = 1$ in a cylindrical tube (Coulliette and Pozrikidis, 1998). Although the steady streamlined shapes adopted by the drops in our simulations are qualitatively similar in the x_2–x_3 plane to those observed in previous experimental (Olbricht and Kung, 1992) and theoretical campaigns (Coulliette and Pozrikidis, 1998) for cylindrical tubes, the steady drop shapes for our channel-flow simulations are symmetric about the channel midplane, but not axisymmetric like those observed for cylindrical tubes, and can be described as "heart-shaped". Unfortunately, experimental studies of deformable drops in planar channels with dimensions comparable to the channel are lacking in the literature to date.

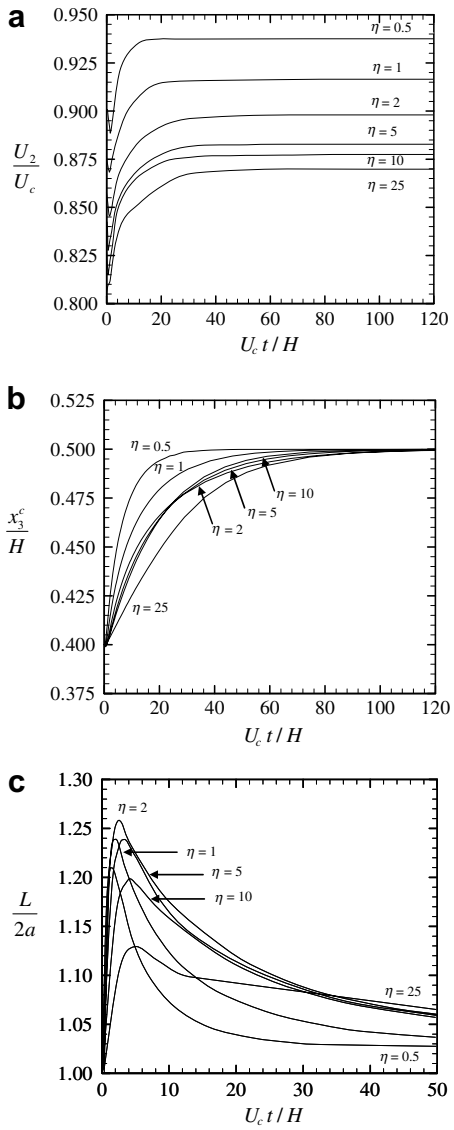

Fig. 7. Trends for the lateral migration of drops with various η, $Ca = 0.5$, and $2a/H = 0.6$. The (a) translational velocities (b) drop centers, and (c) tip-to-tip drop lengths are plotted as functions of time.

We have extended our boundary-integral calculations to study drop migration for non-matching viscosities. Fig. 7 shows results for a range of viscosity ratios with fixed $Ca = 0.5$. A typical calculation with $N_{\triangle} = 3840$ and $\eta = 2$ required approximately 6 h to reach $U_c t/H = 50$, using a AMD Athlon 2800+ processor under Visual Fortran. In Fig. 7a, the translational velocities parallel to the channel walls are plotted versus time for several drops having different viscosity ratios. With increasing viscosity ratio, the average drop velocity parallel to the channel wall, U_2, decreases due to the increased hydrodynamic resistance. In Fig. 7b, the drop center positions (surface centroid, x_3^c) are plotted with time. In all cases, the drop migrates towards the centerplane of the channel, where it reaches and maintains a steady-state shape and velocity. The rate at which the drops migrate towards the channel center depends on the capillary number and the viscosity ratio, both of which influence the drop deformation. When the capillary number is fixed, increasing the viscosity ratio from $\eta = 0.5$ to 1 results in a reduced migration velocity, due to higher hydrodynamic resistance. For large viscosity ratios (e.g. $\eta = 25$), both the longitudinal and transverse velocities are relatively low, due to the diminished internal flow. However, over the range $\eta = 2$–10, non-monotonic behavior is observed for the cross-channel (transverse) migration velocities. This behavior can be explored with the aid of several important observations from Fig. 7c, which shows the maximum drop elongation (relative to the spherical drop diameter) as a function of time. For the range of η considered here, the degree of deformation for steady drop shapes increases monotonically with increasing viscosity ratio, but the trends for the dynamic deformation are not as simple. In all cases, the drops initially elongate as they are deformed by the flow, and then relax toward a more compact steady shape as the tail retracts. During the initial short-time elongation phase, low-viscosity drops deform most rapidly (and reach maximum elongation in the shortest time), because they offer less viscous resistance

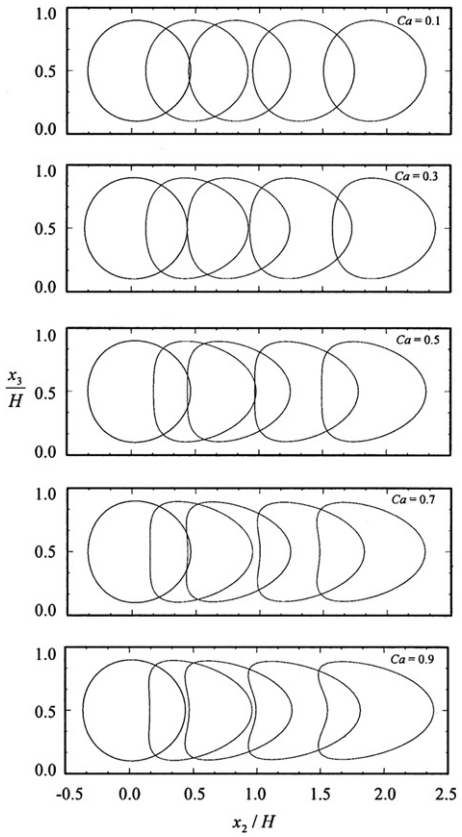

Fig. 8. Transient drop shapes (contours) for deformable drops with $\eta = 1.0$, $2a/H = 0.8$ for a series of $Ca = 0.1$, 0.3, 0.5, 0.7, and 0.9 as a function of position in the channel. The drops are initially spherical and placed in the center of the channel ($x_3/H = 0.5$). The drop shapes are given at $U_c t/H = 0.05$, 1.0, 2.0, 3.0, and 4.5 (left to right) for each value of capillary number.

to dynamic deformation. In contrast, after the relaxation phase, high-viscosity drops reach the greatest deformation (albeit slowly). Since, in general, the rate of lateral migration increases with increasing deformation, the low-viscosity drops move most rapidly towards the channel centerplane during the initial phase, but higher-viscosity drops may migrate more rapidly towards the centerplane during the latter phase. In particular, Fig. 7b shows a cross-over at $U_c t/H \sim 25$, where the drops with $\eta = 5$ and 10 migrate faster across streamlines after this time than does the drop with $\eta = 2$.

For drop motion along the channel center, we have observed steady shapes that have a tapered front and a blunt trailing surface for small *Ca*. As *Ca* is increased, the drop elongates in the direction of the Poiseuille flow, the shape of the trailing surface becomes more complicated, and, eventually, a non-axisymmetric posterior dimple develops. Fig. 8 shows transient drop profiles (two-dimensional slices in the plane $x_1 = 0$) for drops initially placed on the channel center with an initial non-deformed spherical diameter of $2a/H = 0.8$ and $\eta = 1$, for a range of capillary numbers. When the capillary number is small, drops tend to maintain a nearly spherical shape. With increasing *Ca*, the drops elongate more and an accompanied increase in the steady longitudinal velocities is observed, due to the (slightly) larger surface clearances. For sufficiently large *Ca*, the curvature of the trailing surface changes sign. For the drop size and viscosity ratio presented in Fig. 8, drops develop and maintain an increasingly pronounced posterior dimple with increasing *Ca* above 0.5, which can be attributed to the parabolic flow indenting the backside of the drop. We find that steady-state drop shapes are obtained with this feature up to $Ca \sim 1.0$. Above this critical *Ca*, the drops continuously deform (eventually causing the numerical code to fail) and breakup is expected. A side view (x_2–x_3) of the three-dimensional meshes for these steady drop shapes is given in Fig. 9. These regular meshes are maintained for long times for subcritical *Ca*, which allow the complicated drop shapes to be resolved using only a moderate number of triangles ($N_\triangle = 3840$). As noted earlier, the steady velocity of a deformable drop between two

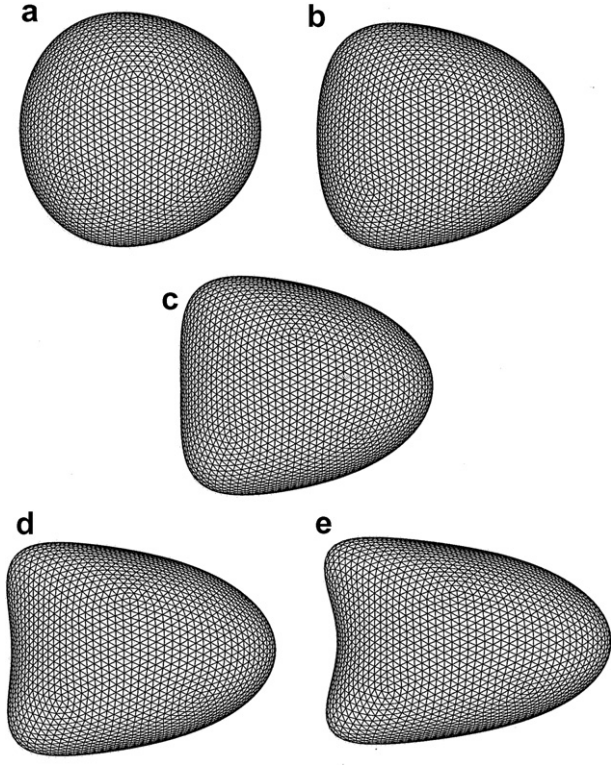

Fig. 9. Three-dimensional meshes for the steady-state shape reached by deformable drops with $\eta = 1.0$ and $2a/H = 0.8$, using $N_\triangle = 3840$ for *Ca* = (a) 0.1, (b) 0.3, (c) 0.5, (d) 0.7, and (e) 0.9.

parallel plane walls is related to the drop shape and viscosity. Compared to viscous drops, bubbles having the same capillary number are less tapered and do not develop these pronounced posterior dimples.

Steady velocities and minimum wall separations are plotted in Fig. 10 for homoviscous drops over a range of drop sizes and capillary numbers. We have included results for cases when $2a/H > 1$, which are discussed further in the next section. When the drops are sufficiently small, they move with the fluid velocity, but the velocity decreases with increasing drop size due to viscous interactions with the walls and the parabolic velocity profile from the imposed Poiseuille flow. The decrease in velocity is greatest for small *Ca*, as the drops deform less and so their edges remain closer to the walls. For larger *Ca*, the decrease in velocity is nearly linear with increasing drop size. Since drop deformability increases with increasing *Ca*, the minimum gap increases, thus lowering the hydrodynamic resistance and resulting in an increased velocity relative to the non-deformed spherical shapes. In contrast to drops with small *Ca*, the minimum drop-to-wall spacing as a function of drop size has a noticeable degree of convexity for larger *Ca*, as shown in Fig 10b, attributable to greater deformation.

Fig. 11 shows steady longitudinal velocities and wall separations for drops with $2a/H = 0.9$ as a function of capillary number for a range of drop-to-medium viscosity ratios. The decreased velocity parallel to the wall with increasing viscosity ratio is due to the reduced internal flow inside the drop. For all viscosity ratios, the velocity increases with increasing *Ca*, as expected. However, the change is greater for the more viscous drops because they are more deformed than inviscid drops at long times over a wide range of drop sizes. When the drop size is comparable to the channel height, the trailing surface of viscous drops may develop symmetric tails that come in close contact with the walls for sufficiently large *Ca*. Such features of highly deformable drops are less pronounced for low-viscosity ratios than for more viscous drops and are discussed in the next section.

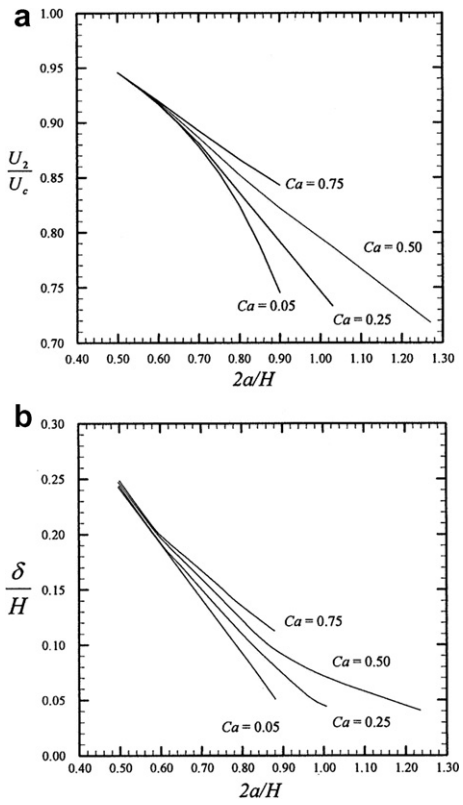

Fig. 10. Steady longitudinal velocities and minimum drop-to-wall spacing for homo viscous drops as a function of non-deformed spherical diameter for a range of capillary numbers.

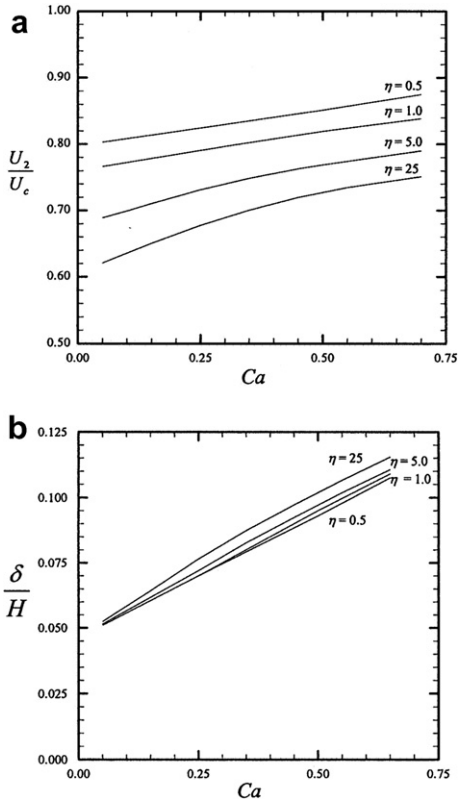

Fig. 11. Steady translational velocities and minimum surface clearances as a function of capillary number for drops with $2a/H = 0.9$ for a range of viscosity ratios.

4.4. Large drops

Simulations involving tightly fitting drops are often computationally challenging, since the drop surface is close to both walls. We present such a challenging case for a deformable drop with $Ca = 0.25$ that is initially placed on the channel midplane and spherical with $2a/H = 0.98$. The longitudinal velocity and the minimum drop-to-wall spacing, δ, are plotted versus time in Fig. 12. Drop shapes are plotted for this case as a function of channel position in Fig. 13a, while the steady shape is shown with shading and contours from the top in Fig. 13b, and from an angled perspective in Fig. 13c. Viscous forces cause the drop to deform in such a way that there is a short period when the drop surface closely approaches the walls, where, as shown in Fig 12b, the minimum gap decreases to about 0.3% of the channel height, which results in the observed decrease in the translational velocity. Interfacial forces then cause the drop edges to move away from the walls, while the external flow stretches the drop along the x_2-direction, and the longitudinal velocity increases as a result. Since the drop contracts along the x_3-axis and moves away from the walls, the drop interface maintains favorable geometric configurations, which foster stable simulations, even when in close proximity to both walls. Near-singularity subtraction is essential in resolving the small surface clearances in such cases. For example, the simulation for Fig. 12 faltered very early ($U_c t/H \sim 1.0$) when the near-singularity subtraction was excluded in the calculations; however, with the subtraction scheme in (15), we are able to extend the calculation to $U_c t/H > 4$, well after a steady-state translational velocity and shape are obtained. In contrast with calculations for rigid spheres (Staben et al., 2003), adaptive surface triangulations were not required for simulations of deformable drops, possibly owing to the lower hydrodynamic resistance in the near-contact zones, when compared to the case of solid particles.

We now consider the case of a drop initially having an ellipsoidal shape and volume greater than a spherical drop that would fit tightly in the channel. The semi-axes of the ellipsoidal drop are initially $[a_1/H, a_2/H,$

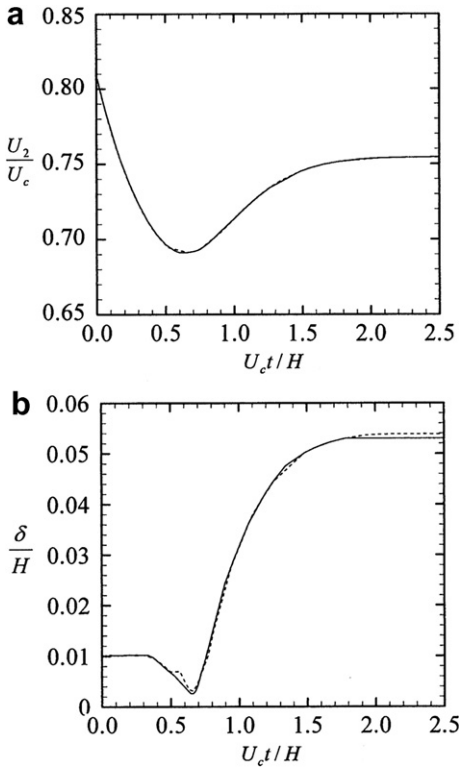

Fig. 12. Simulation results for two levels of triangulation, $N_\triangle = 8640$ (dashed line) and 15 360 (solid line) for (a) the longitudinal velocity and (b) the minimum drop-to-wall spacing, δ, as functions of time, with $2a/H = 0.98$, $Ca = 0.25$, and $\eta = 1$.

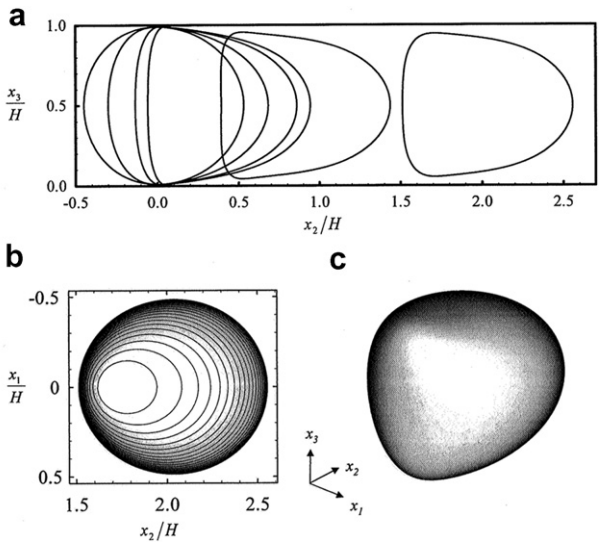

Fig. 13. Contours of a three-dimensional drop showing the deformation of a drop with dimensions comparable to the channel height ($2a/H = 0.98$) with $Ca = 0.25$ and $\eta = 1$, for $U_c t/H = 0.1$, 0.2, 0.5, 0.6, 1.2, and 2.7 (left to right) in (a). The top view of the steady drop shape is given in (b) with shading and contours. The steady shape from an angled view with shading is given in (c).

$a_3/H] = [1.6, 1.6, 0.8]$, resulting in a drop diameter that is 27% larger than that of a spherical drop that would contact both walls. Fig. 14 shows drop contours for a homoviscous drop with $Ca = 0.5$, using $N_\triangle = 11\,520$.

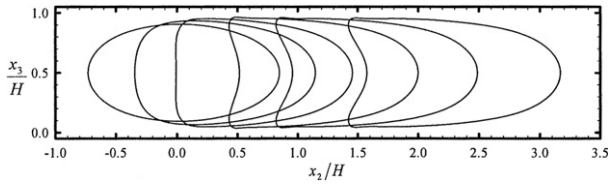

Fig. 14. Contours of a three-dimensional drop with $2a/H = 1.27$, $\eta = 1$, and $Ca = 0.5$ showing the deformation from its initial ellipsoidal shape over time with $U_c t/H = 0.1$, 0.4, 0.8, 1.2, 1.6, and 2.0 (left to right).

Initially, the drop contracts slightly due to interfacial tension, and is then stretched by the external flow. The steady shape adopted by the initially ellipsoidal-shaped drop is similar to those that are initially spherical in shape (cf. Fig. 8); the external Poiseuille flow tends to form a posterior dimple, which becomes more pronounced as the viscous forces become more dominant. For larger drops, we expect the shape of the posterior dimple will heavily influence the drop motion, since the average surface clearance is expected to vary little over the length of the drop.

We now examine the effect of varying the viscosity ratio for tightly fitting drops. Fig. 15 gives results for the translational velocities as a function of time for $\eta = 0.5$, 1.0, and 2.0 with fixed $Ca = 0.5$. As the viscosity ratio is increased, the steady drop velocity decreases. The steady-state contours for these drops are compared in Fig. 16. As expected, the long-time deformability increases with increasing viscosity ratio. Although the minimum gap decreases with increasing η, the average surface clearance is nearly independent of η. The minimum drop-to-wall spacing is located near the trailing edge of the drops, where a puckered end develops,

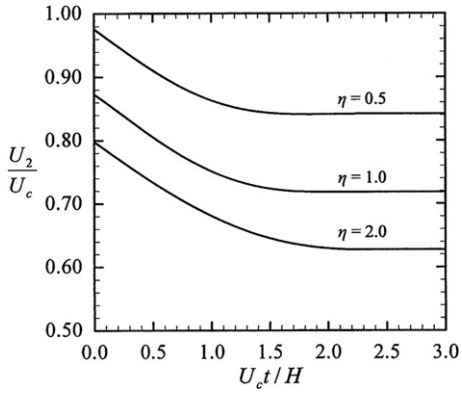

Fig. 15. Longitudinal velocities of initially ellipsoidal-shaped drops ($2a/H = 1.27$) as functions of time for $Ca = 0.5$ and various η.

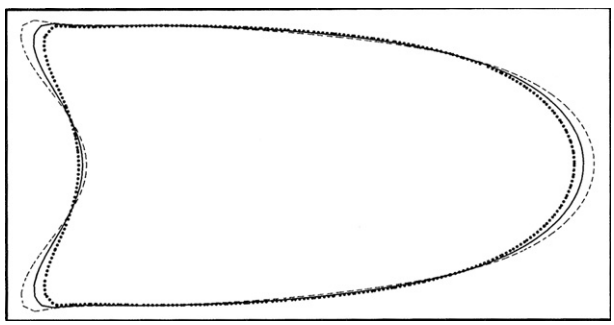

Fig. 16. Steady drop shapes shown as contours for $Ca = 0.5$ and $2a/H = 1.27$ with viscosity ratios, $\eta = 2$ (dashed), $\eta = 1$ (solid), and $\eta = 0.5$ (dotted).

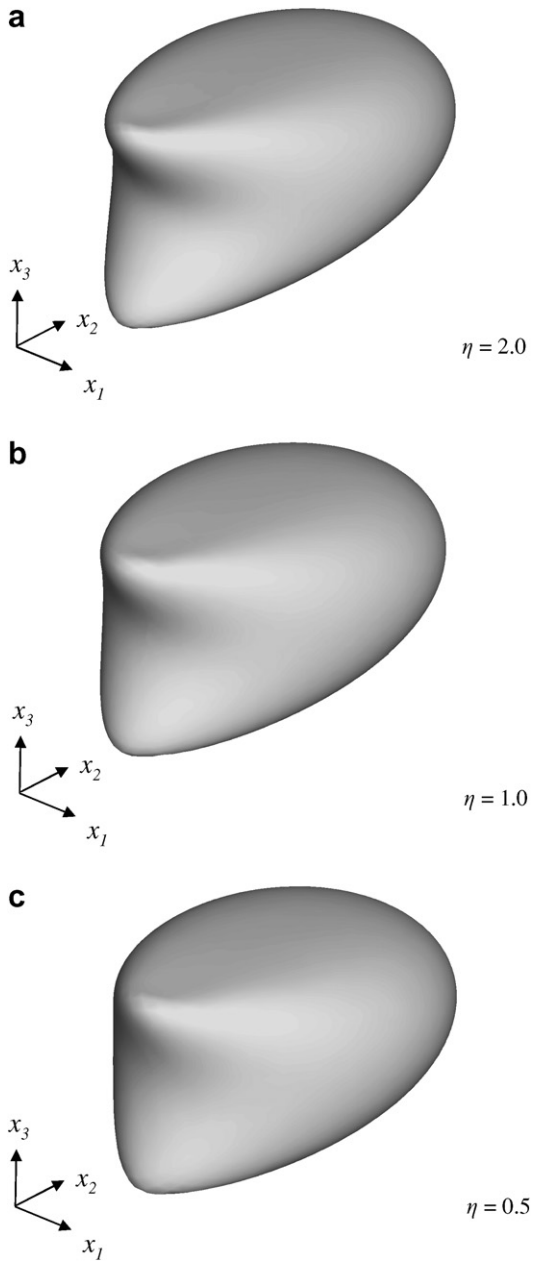

Fig. 17. Three-dimensional steady-state drop shapes with shading with $Ca = 0.5$ and $2a/H = 1.27$ for (a) $\eta = 2$, (b) $\eta = 1$, and (c) $\eta = 0.5$.

which is more noticeable for $\eta = 2$ than for $\eta = 1$ or 0.5. Fig. 17 gives the three-dimensional drop shapes with shading, which shows the complicated shapes obtained by these drops. As the drop viscosity is increased, the flow inside the drop takes a more dominant role in influencing the drop shape, as can be argued by considering the normal stress balance across the interface (Olbricht and Kung, 1992). Further increases in η result in the drop tails becoming progressively more elongated and proximate to the walls. We were unable to conduct simulations for drops of the same size and capillary number beyond $\eta \sim 6$, since the tails at the trailing surface became too elongated, which may be a sign of breakup. Experimentally obtained critical capillary numbers for large drops in cylindrical tubes have been reported to decrease with increasing viscosity ratio (Olbricht and Kung, 1992).

5. Concluding remarks

The kinematics of a freely suspended drop between two parallel walls subject to a Poiseuille flow have been examined here for a wide range of drop sizes, capillary numbers, and viscosity ratios. Deformable drops migrate away from the closest wall, and the preferred steady location was found to be centered on the channel midplane ($x_3/H = 0.5$), where the drop eventually maintains a non-spherical steady shape for finite Ca; the deviations from the spherical shape were found to be an increasing function of Ca. Steady shapes for viscous drops are more elongated than for bubbles and exhibit pronounced posterior dimples. For drops with non-deformed spherical diameter exceeding the channel height, as the viscosity ratio is increased, the drop-to-wall spacing remains nearly uniform across the length of the drop, but the trailing interface becomes more deformed and proximate to the walls when Ca is fixed. The component of the drop velocity parallel to the walls is also an increasing function of Ca over the range examined.

When Ca is sufficiently large, the drop is expected to continually deform in an unrestricted manner, without reaching a steady shape. To establish a critical capillary number, above which this unrestricted deformation and breakup occur, we must be able to resolve very large drop deformations. Presently, we are unable to accomplish this task using the current version of the code, since the curvature calculation becomes ill-conditioned on a highly stretched mesh. This difficulty produces either slowly convergent calculations or, in some cases, operational failure of the code. As an example of the difficulties encountered for large deformations, Fig. 18 gives two of the computed drop shapes at time $U_c t/H = 1.83$ using two different mesh

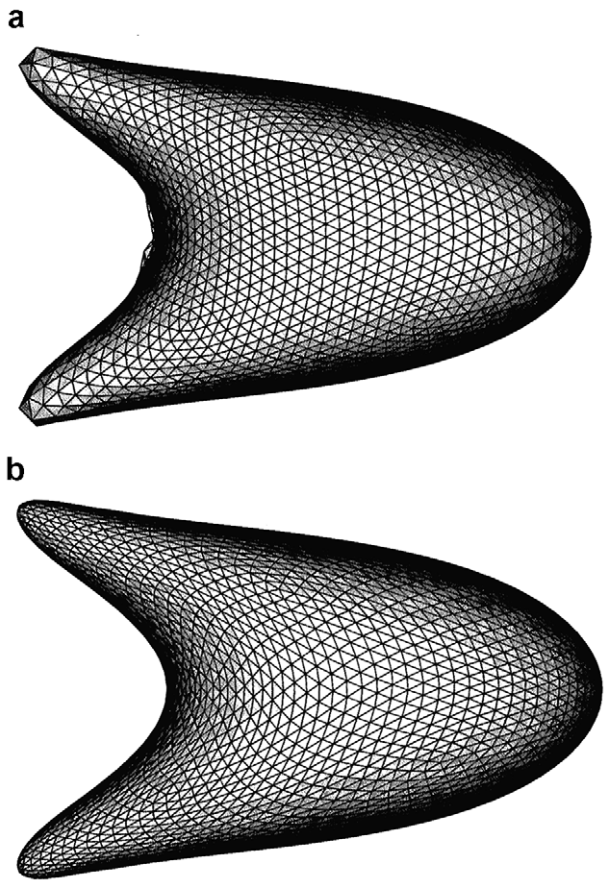

Fig. 18. Simulation results at $U_c t/H = 1.83$ for a drop with $2a/H = 0.9$, $\eta = 1$, and $Ca = 0.95$ for using a (a) simple and (b) more advanced mesh-stabilization algorithm.

stabilization techniques, both with $2a/H = 0.9$, $\eta = 1$, and $Ca = 0.95$, using $N_{\triangle} = 6000$. When the simpler stabilization technique is employed (Zinchenko et al., 1997), the calculation begins to show signs of instability. However, when the more advanced mesh-stabilization technique (Zinchenko et al., 1999) is used, more triangles are retained in the areas of high curvature in Fig. 18b. This approach to mesh stabilization allows the calculation to continue for a short time where the drop continues to deform. The shapes given in Fig. 18 represent the upper-stability limit for calculations due to the ill-conditioned curvature calculation, inherent for drops undergoing large deformations. To overcome such difficulties, a method that is less sensitive to the curvature calculation, or perhaps even recasting the boundary integrals into a form without curvature, which has been demonstrated for drops in an unbounded fluid (Zinchenko et al., 1999), would be required. To study tightly fitting drops that are also highly elongated, multipole acceleration of the boundary integrals (Zinchenko and Davis, 2000, 2005), which affords feasible calculations for drop surfaces with many triangles, e.g. $N_{\triangle} \sim 10^4$–10^5, is likely to be necessary to simultaneously resolve complicated drop shapes and small surface clearances.

Our boundary-integral algorithm solution method utilizes the Green's function for the space between two parallel walls, thus avoiding discretization of the channel walls, and an economical scheme for evaluating the two-wall interaction term, which is the most computationally burdensome portion of the code, was developed. This calculation scheme has enabled accelerations of several orders of magnitude, when compared to the direct evaluation of the regularized Fourier–Bessel integrals. Near-singularity subtractions greatly improve the convergence of the algorithm for small surface clearances. The algorithm allows for arbitrary drop-to-medium viscosity ratios and drop diameters close to the channel dimensions to be considered, and fast convergence of simple iterations is observed for drop-to-wall spacings of less than 0.5% of the channel height when $\eta = \mathrm{O}(1)$. Furthermore, the algorithm is quite robust in resolving these small clearances without the aid of adaptive surface triangulations (Staben et al., 2003). The choice of simple iterations, based on successive substitutions, over a more advanced iterative scheme, such as biconjugate gradient or minimal-residual iterations, was made to not over-complicate the code, leaving more difficult cases of extreme η for future investigation. In addition to the above, a natural extension of this work would be to encompass buoyant drops or incorporate other conservative body forces, which could be made by simple modifications to the existing code.

Acknowledgements

This work was supported by the Defense Advanced Research Projects Agency through the Air Force Office of Scientific Research and the Graduate Assistantships in Areas of National Need program of the Department of Education. A.Z.Z. also acknowledges the Donors of the American Chemical Society Petroleum Research Fund for partial support of this research.

Appendix A. Economical evaluation of the two-wall interaction term in the Green's function

The central aim of the current work is to develop efficient boundary-integral calculations that permit the study of the creeping motion of a deformable drop between two parallel plane walls. The Green's function for the case of one wall (i.e. $\mathbf{G}_0^l + \mathbf{G}_{\mathrm{LW}}^l$) (Blake, 1971) corresponds to the solution in the entire half-space $x_3 > 0$ or when $H \to \infty$. In order to consider a channel consisting of two walls, repeated reflections must be taken to satisfy the no-slip conditions on both walls simultaneously. The resulting Green's function for the domain between two parallel walls was originally derived by Liron and Mochon (1976) in terms of infinite Fourier–Bessel integrals. Improvements to the original solution were made by regularizing the Fourier–Bessel integrals, eliminating the slow convergence (Staben et al., 2003). However, direct calculation of the regularized integrals at every timestep in dynamical simulations still imposes a prohibitive computational demand. To circumvent such expensive calculations, we have devised a scheme that involves double Taylor expansions of the two-wall interaction term, $\widehat{\mathbf{G}}^l(\mathbf{x};\mathbf{y})$, about the drop center, $\mathbf{x} = \mathbf{y} = \mathbf{x}_{\mathrm{c}}$. In this way, the necessary repeated reflections are assimilated into the boundary-integral equation, permitting dynamical simulations of deformable drops, without greatly decelerating the code.

The smooth parts of the fundamental solution for the velocity and pressure fields (Staben et al., 2003; Liron and Mochon, 1976) are represented as

$$\widehat{G}_j^l(\mathbf{x};\mathbf{y}) = \hat{w}_j^l + \hat{v}_j^l, \tag{A1}$$

$$\hat{p}^l(\mathbf{x};\mathbf{y}) = \hat{q}^l + \hat{s}^l. \tag{A2}$$

The expressions for the velocity are most conveniently handled separately for $l=\beta=1,2$ from cases when $l=3$. Firstly, the velocity and pressure fields when $j=\alpha=1,2$ are

$$\hat{w}_\alpha^\beta + \hat{v}_\alpha^\beta = \frac{1}{4\pi}\left[\delta_{\alpha\beta}\int_0^\delta J_0(\lambda\rho)\widehat{B}_1(\lambda)\mathrm{d}\lambda + \frac{r_\alpha r_\beta}{\rho}\int_0^\infty \lambda J_1(\lambda\rho)\widehat{A}_1(\lambda)\mathrm{d}\lambda - \frac{\partial}{\partial r_\beta}\frac{r_\alpha}{\rho}\int_0^\infty \lambda J_1(\lambda\rho)\widehat{A}_1(\lambda)\mathrm{d}\lambda\right], \tag{A3}$$

$$\hat{p}^\beta(\mathbf{x};\mathbf{y}) = \frac{1}{2\pi}\left\{\frac{r_\beta}{\rho}\int_0^\infty J_1(\lambda\rho)[\lambda\widehat{B}_1(\lambda) + \widehat{A}_5(\lambda)]\mathrm{d}\lambda\right\}, \tag{A4}$$

when $l=3$ and $j=\alpha=1,2$ the velocity components become

$$\hat{v}_\alpha^3 + \hat{w}_\alpha^3 = \frac{1}{4\pi}\left\{r_\alpha\int_0^\infty \lambda J_0(\lambda\rho)\widehat{B}_4(\lambda)\mathrm{d}\lambda - \frac{\partial}{\partial r_\alpha}\int_0^\infty J_0(\lambda\rho)[\widehat{A}_3(\lambda) + \widehat{A}_4^{l=3}(\lambda)]\mathrm{d}\lambda\right\}, \tag{A5}$$

and for indices $l=\alpha$ and $j=3$,

$$\hat{v}_3^\alpha + \hat{w}_3^\alpha = \frac{1}{4\pi}\left\{r_\alpha\int_0^\infty \lambda J_0(\lambda\rho)\widehat{B}_4(\lambda)\mathrm{d}\lambda - \frac{\partial}{\partial r_\alpha}\int_0^\infty J_0(\lambda\rho)[\widehat{A}_3(\lambda) + \widehat{A}_4^{l=3}(\lambda)]\mathrm{d}\lambda\right\}. \tag{A6}$$

Finally, for the case when $l=j=3$, the expressions for the velocity and pressure are

$$\hat{v}_3^3 + \hat{w}_3^3 = \frac{1}{4\pi}\left\{\int_0^\infty J_0(\lambda\rho)\widehat{A}_2(\lambda)\mathrm{d}\lambda + \int_0^\infty J_0(\lambda\rho)\widehat{B}_1(\lambda)\mathrm{d}\lambda - \int_0^\infty \lambda J_0(\lambda\rho)\widehat{B}_3(\lambda)\mathrm{d}\lambda\right\}, \tag{A7}$$

$$\hat{p}^3(\mathbf{x};\mathbf{y}) = \frac{1}{2\pi}\left\{\int_0^\infty J_0(\lambda\rho)[\lambda\widehat{B}_4(\lambda) + \widehat{B}_6(\lambda)]\mathrm{d}\lambda\right\}, \tag{A8}$$

where $\rho^2 = r_1^2 + r_2^2$, $r_1 = x_1 - y_1$, and $r_2 = x_2 - y_2$.

The slow convergence of the original Fourier–Bessel integrals, when $\mathbf{x}\approx\mathbf{y}$ and/or when $\mathbf{x}$ and $\mathbf{y}$ are close to the same wall, is remedied by subtraction of the terms responsible for the poor numerical behavior from the $A(\lambda)$- and $B(\lambda)$-coefficients of Liron and Mochon (1976). The resulting regularized Fourier–Bessel integrals (Staben et al., 2003), involving functions of x_3 and $h=y_3$, are expressed using coefficients with hats

$$\widehat{A}_1(\lambda) = A_1(\lambda) - \{hx_3\mathrm{e}^{-\lambda(h+x_3)} + (h-1)(x_3-1)\mathrm{e}^{\lambda(h+x_3-2)}\}, \tag{A9}$$

$$\widehat{A}_2(\lambda) = A_2(\lambda) - \lambda^2\{-hx_3\mathrm{e}^{-\lambda(h+x_3)} - (h-1)(x_3-1)\mathrm{e}^{\lambda(h+x_3-2)}\}, \tag{A10}$$

$$\widehat{A}_3(\lambda) = A_3(\lambda) - \{h\mathrm{e}^{-\lambda(h+x_3)} + (h-1)\mathrm{e}^{\lambda(h+x_3-2)}\}, \tag{A11}$$

$$\widehat{A}_4(\lambda) = A_4(\lambda) - \lambda(\delta_{j3}-\delta_{k3})\{hx_3\mathrm{e}^{-\lambda(h+x_3)} - (h-1)(x_3-1)\mathrm{e}^{\lambda(h+x_3-2)}\}, \tag{A12}$$

$$\widehat{A}_5(\lambda) = A_5(\lambda) - \lambda^2\{h\mathrm{e}^{-\lambda(h+x_3)} - (h-1)\mathrm{e}^{\lambda(h+x_3-2)}\}, \tag{A13}$$

$$\widehat{A}_6(\lambda) = A_6(\lambda) - \lambda^2\{-h\mathrm{e}^{-\lambda(h+x_3)} - (h-1)\mathrm{e}^{\lambda(h+x_3-2)}\}, \tag{A14}$$

$$\widehat{B}_1(\lambda) = B_1(\lambda) - \frac{1}{2}\{\mathrm{e}^{\lambda(h-x_3)} - \mathrm{e}^{\lambda(h+x_3-2)} - \mathrm{e}^{-\lambda(h+x_3)}\}, \tag{A15}$$

$$\widehat{B}_3(\lambda) = B_3(\lambda) - \frac{1}{2}\{(h-x_3)\mathrm{e}^{\lambda(h-x_3)} - (h+x_3-2)\mathrm{e}^{\lambda(h+x_3-2)} + (h+x_3)\mathrm{e}^{-\lambda(h+x_3)}\}, \tag{A16}$$

$$\widehat{B}_4(\lambda) = B_4(\lambda) - \frac{1}{2}\{\mathrm{e}^{\lambda(h-x_3)} + \mathrm{e}^{\lambda(h+x_3-2)} - \mathrm{e}^{-\lambda(h+x_3)}\}. \tag{A17}$$

Essential to the efficient calculation of the two-wall interaction term is the introduction of an auxiliary field, $g_j^l(\mathbf{x};\mathbf{y}) = G_j^l(\mathbf{x};\mathbf{y}) - \frac{1}{2}p^l(\mathbf{x})x_j$, which can be shown to be a harmonic function with respect to $\mathbf{x}$ (i.e. $\nabla_x^2\mathbf{g}^l(\mathbf{x};\mathbf{y}) = \mathbf{0}$). For any harmonic function, $Y(\mathbf{x})$, the Taylor expansion has a special form,

$$Y(\mathbf{x}) = \sum_{v=0}^{\infty}\sum_{\mu=-v}^{v} \partial_{v,\mu} Y(\mathbf{x})|_{\mathbf{x}=\mathbf{x}_c}\, Z_{v,\mu}(\mathbf{x}-\mathbf{x}_c), \tag{A18}$$

where $Z_{v,\mu}(\mathbf{x}-\mathbf{x}_c)$ is a special solid spherical harmonic that depends only on $(\mathbf{x}-\mathbf{x}_c)$ (Zinchenko and Davis, 2000), and the derivative operator $\partial_{v,\mu}$ is,

$$\partial_{v,\mu} = [D_1 - \mathrm{i}D_2]^{\mu} D_3^{v-\mu} \quad \text{for } \mu \geqslant 0, \tag{A19}$$

$$\partial_{v,\mu} = (-1)^{\mu}[D_1 + \mathrm{i}D_2]^{-\mu} D_3^{v-|\mu|} \quad \text{for } \mu < 0, \tag{A20}$$

where $D_j = \partial/\partial x_j$ for $j = 1,2,3$, and $\mathrm{i} = \sqrt{-1}$.

Consider a neutrally buoyant drop with a viscosity matching the surrounding fluid, when the double-layer term (3) vanishes. The contribution of the two-wall interaction term to the boundary-integral (2) can be expressed in discrete form as

$$\int_s 2\sigma k(\mathbf{x})\mathbf{n}(\mathbf{x})\cdot\widehat{\mathbf{G}}^l(\mathbf{x};\mathbf{y})\mathrm{d}S_{\mathbf{x}} = \sum_{\mathbf{x}_n\in S}\mathbf{W}(\mathbf{x}_n)\cdot\widehat{\mathbf{G}}^l(\mathbf{x}_n;\mathbf{y}), \tag{A21}$$

where $\mathbf{x}_n$ are the triangle vertices on S, and $\mathbf{W}(\mathbf{x}_n) = 2\sigma k(\mathbf{x}_n)\mathbf{n}(\mathbf{x}_n)\Delta S_n$ are the associated weights. For arbitrary viscosity ratios, the single-layer portion of the boundary-integral equation containing the interaction term is expected to have a more pronounced effect on the solution for velocity than the double-layer term. Substituting the relation $\widehat{G}_j^l(\mathbf{x};\mathbf{y}) = \hat{g}_j^l(\mathbf{x};\mathbf{y}) + \frac{1}{2}\hat{p}^l(\mathbf{x})x_j$ in (A21) and using the expansion (A18) for $\hat{g}$ and $\hat{p}$ yields

$$\sum\nolimits_{\mathbf{x}_n\in S}\mathbf{W}(\mathbf{x})\cdot\widehat{\mathbf{G}}^l(\mathbf{x};\mathbf{y}) = 2\,Re\left\{\sum_{v=0}^{\infty}\sum_{\mu=0}^{v}\mathscr{D}_{v,\mu,j}\partial_{v,\mu}\hat{g}_j^l(\mathbf{x}_c;\mathbf{y}) + \frac{1}{2}\sum_{v=0}^{\infty}\sum_{\mu=0}^{v}\partial_{v,\mu}\hat{p}^l(\mathbf{x}_c;\mathbf{y})\left[\mathscr{D}_{v,\mu,j}(\mathbf{x}_c-\mathbf{y})_j + E_{v,\mu}\right]\right\}, \tag{A22}$$

where Re denotes the real parts of the braced argument. The "far-field moments", $\mathscr{D}_{v,\mu,j}$ and $E_{v,\mu}$, which are pre-calculated to expedite calculations, are defined as

$$\mathscr{D}_{v,\mu,j} = \sum_{\mathbf{x}_n\in S} Z_{v,\mu}(\mathbf{x}_n-\mathbf{x}_c)W_j(\mathbf{x}_n), \tag{A23}$$

$$E_{v,\mu} = \sum_{\mathbf{x}_n\in S} Z_{v,\mu}(\mathbf{x}_n-\mathbf{x}_c)W_j(\mathbf{x}_n)(x_n-x_c)_j, \tag{A24}$$

where it is understood that for $\mu = 0$, both quantities are additionally multiplied by 1/2. Calculations are further facilitated by reordering the sums, thereby removing dependencies of the $\mathbf{y}$ point when appropriate, and using sufficient truncation bounds for each of the sums. The idea here is simple: compute the coefficients using a Taylor series about a single point, rather than performing calculations for every $(\mathbf{x},\mathbf{y})$ pair.

When $l = \beta =$ and $j = \alpha$ the auxiliary function is

$$\hat{g}_\alpha^\beta(\mathbf{x};\mathbf{y}) = \widehat{G}_\alpha^\beta(\mathbf{x};\mathbf{y}) - \frac{1}{2}\hat{p}^\beta(x;y)\boldsymbol{r}_\alpha = \frac{1}{4\pi}\left\{\delta_{\alpha\beta}\left(\int_0^\infty J_0(\lambda\rho)\widehat{B}_1(\lambda)\mathrm{d}\lambda - \frac{1}{\rho}\int_0^\infty \lambda J_1(\rho\lambda)\widehat{A}_1(\lambda)\mathrm{d}\lambda\right)\right.$$
$$\left. - \frac{r_\alpha r_\beta}{\rho}\int_0^\infty J_1(\lambda\rho)\widehat{A}_5(\lambda)\mathrm{d}\lambda - 2r_\alpha r_\beta\frac{\partial}{\partial(\rho^2)}\left[\frac{1}{\rho}\int_0^\infty \lambda J_1(\rho\lambda)\widehat{A}_1(\lambda)\mathrm{d}\lambda\right]\right\}. \tag{A25}$$

The mth order Bessel function can be expanded as (Abramowitz and Stegun, 1972):

$$J_m(\lambda\rho) = \sum_{k=0}^{\infty} C_k^m(\lambda\rho)^{2k+m}, \tag{A26}$$

$$C_k^m = \frac{(-1)^k}{2^{2k+m}k!(m+k)!}. \tag{A27}$$

The derivative operator $\partial_{v,\mu} = [D_1 - \mathrm{i}D_2]^{\mu} D_3^{v-\mu}$ is then applied to the appropriate combinations of pressure and velocity (e.g. in (A25)).

Noting $[D_1 - \mathrm{i}D_2]^{\mu}(\rho^2) = [D_1 - \mathrm{i}D_2]^{\mu}(r_1^2 + r_2^2)$, where $\mathbf{r} = \mathbf{x} - \mathbf{y}$, and $[D_1 - \mathrm{i}D_2]^{\mu}(\rho^{2k}) = \rho^{2(k-\mu)} 2^{\mu}\, (r_1 - \mathrm{i}r_2)^{\mu}\, k!/k-\mu)!$, the following coefficients are introduced for brevity:

$$a_k^{(1)} = \frac{(-1)^k}{2^{2k+1}(k+1)!}, \quad a_k^{(0)} = \frac{(-1)^k}{2^{2k}k!}, \quad \Delta h_m = \frac{(h - x_3^{\mathrm{c}})^m}{m!},$$
$$b_{k,\mu} = \frac{2^{\mu}}{(k-\mu)!}\rho^{2(k-\mu)}(r_1 - \mathrm{i}r_2)^{\mu}. \tag{A28}$$

Adhering to the above notations and applying the required operations to (A25) gives

$$\sum_{v=0}^{\infty}\sum_{\mu=0}^{v} \mathscr{D}_{v,\mu,\alpha}\partial_{v,\mu}\hat{g}_{\alpha}^{\beta}(\mathbf{x}_{\mathrm{c}};\mathbf{y})$$
$$= \sum_{m=0}^{\infty}\Delta h_m \sum_{\mu=0}^{\infty}\sum_{k=\mu}^{\infty} b_{k,\mu}K_{\mu,m,k,\beta}^{(1)} - \sum_{m=0}^{\infty}\Delta h_m \sum_{\mu=0}^{\infty}\sum_{k=\mu-2}^{\infty}\{r_\alpha r_\beta b_{k,\mu} + \mu[\delta_{\alpha 1}r_\beta + \delta_{\beta 1}r_\alpha - \mathrm{i}(\delta_{\beta 2}r_\alpha + \delta_{\alpha 2}r_\beta)]b_{k,\mu-1}$$
$$+\mu(\mu-1)[\delta_{\alpha 1}\delta_{\beta 1} - \delta_{\alpha 2}\delta_{\beta 2} - i(\delta_{\alpha 1}\delta_{\beta 2} + \delta_{\alpha 2}\delta_{\beta 1})]b_{k,\mu-2}\}K_{\mu,m,k,\alpha}^{(2)}, \tag{A29}$$

$$K_{\mu,m,k,\beta}^{(1)} = \frac{1}{4\pi}\sum_{v=\mu}^{\infty}\mathscr{D}_{v,\mu,\beta}\left[a_k^{(0)}\int_0^{\infty}\lambda^{2k}D_h^m D_{x_3}^{v-\mu}\widehat{A}_1(\lambda)\mathrm{d}\lambda - a_k^{(1)}\int_0^{\infty}\lambda^{2K+2}D_h^m D_{x_3}^{v-\mu}\widehat{B}_1(\lambda)\mathrm{d}\lambda\right], \tag{A30}$$

$$K_{\mu,m,k,\alpha}^{(2)} = \frac{1}{4\pi}\sum_{v-\mu}^{\infty}\mathscr{D}_{v,\mu,\alpha}\left[a_k^{(1)}\int_0^{\infty}\lambda^{2k+1}D_h^m D_{x_3}^{v-\mu}\widehat{A}_5(\lambda)\mathrm{d}\lambda + 2a_{k+1}^{(1)}\int_0^{\infty}\lambda^{2k+4}D_h^m D_{x_3}^{v-\mu}\widehat{A}_1(\lambda)\mathrm{d}\lambda\right], \tag{A31}$$

where now $\mathbf{r} = \mathbf{x}_{\mathrm{c}} - \mathbf{y}$ and the derivatives of the hat-coefficients (i.e. (A9)–(A17) with respect to x_3 and h are evaluated at $h = x_3 = x_3^{\mathrm{c}}$. The integrands in (A30) and (A31) depend only on x_3^{c} and the integration variable λ, and are independent of $\mathbf{y}$. Although the above expressions may appear to be more unwieldy than the original integrals, one should note that (A30) and (A31) are independent of $\mathbf{y}$, and the integrals in (A29) and (A30) are rapidly convergent; typically values of λ, less than about 7–8 suffice, requiring only a modest number of integration subintervals. The summations in (A29) are subject to strict truncation bounds to retain a given maximum power of $\mathbf{r}$, which dictates the number of required terms for summation over all indices. Furthermore, the only quantities that depend on $\mathbf{y}$ are Δh_m, $b_{k,\mu}$ and $\mathbf{r}$. All other quantities are calculated only once every half-timestep. The remaining computations involve the terms $\hat{g}_3^3(\mathbf{x};\mathbf{y})$, $\hat{g}_3^{\alpha}(\mathbf{x};\mathbf{y}$, $\hat{g}_{\alpha}^3(\mathbf{x};\mathbf{y})$, $\hat{p}^{\alpha}(\mathbf{x};\mathbf{y})$, and $\hat{p}^3(\mathbf{x};\mathbf{y})$, which follow a similar methodology as given above.

The numerical accuracy of the Taylor expansions was checked against direct calculations involving the regularized Fourier–Bessel integrals, and it was found that the leading-order summation index was m, which involves the term Δh_m. For the most demanding cases when the drop is close to both walls, convergence was achieved with m in the range of 10–15, depending on $(\mathbf{x} - \mathbf{x}_{\mathrm{c}})$ and the proximity of the interface to both walls. Calculation of the interaction term in this manner reduces simulation times for a modest number of triangles to 4–12 h on a PC, as opposed to a few weeks for direct calculation of the Fourier–Bessel integrals. To apply this methodology to highly elongated drops, a drop would need to be partitioned into compact blocks (Zinchenko and Davis, 2000) before Taylor expansions about the block centers are made. Such a generalization, however, was not pursued in the current study limited to moderately large, subcritical deformations. Our findings show that even for drops in close proximity to both walls, the two-wall interaction term contributes relatively little to the overall solution for the cases examined.

References

Abramowitz, M., Stegun, I.A., 1972. Handbook of Mathematical Functions with Formulas, Graphs, & Mathematical Tables. Dover, New York.

Bhattacharya, S., Blawzdziewicz, J., 2002. Image system for Stokes-flow singularity between two parallel planar walls. J. Math. Phys. 43, 5720.

Blake, J.R., 1971. A note on the image system for a stokeslet in a no-slip boundary. Proc. Cam. Philos. Soc.-Math. Phys. Sci. 70, 303.

Chen, K.H., Keh, P.Y., 2001. Slow motion of a droplet between two parallel walls. Chem. Eng. Sci. 56, 6863–6871.
Coulliette, C., Pozrikidis, C., 1998. Motion of an array of drops through a cylindrical tube. J. Fluid Mech. 358, 1–28.
Cristini, V., Blawzdziewicz, J., Loewenberg, M., 1998. Drop breakup in three-dimensional viscous flows. Phys. Fluids 10, 1781–1783.
Cristini, V., Blawzdziewicz, J., Loewenberg, M., 2001. An adaptive mesh algorithm for evolving surfaces: simulations of drop breakup and coalescence. J. Comput. Phys. 168, 445–463.
DeBisschop, K.M., Miksis, M.J., Eckmann, D.M., 2002. Bubble rising in an inclined channel. Phys. Fluids 14, 93–106.
Ganatos, P., Pfeffer, R., Weinbaum, S., 1980. A strong interaction theory for the creeping motion of a sphere between plane parallel boundaries. Part 2 Parallel motion. J. Fluid Mech. 99, 755–783.
Hodges, S.R., Jensen, O.E., Rallison, J.M., 2004. The motion of a viscous drop through a cylindrical tube. J. Fluid Mech. 501, 279–301.
Kim, S., Karrila, S.J., 1991. Microhydrodynamics: Principles and Selected Applications. Butterworths-Heinemann, Boston, MA.
Liron, N., Mochon, S., 1976. Stokes flow for a stokes-let between two parallel flat plates. J. Eng. Math. 10, 287.
Martinez, M.J., Udell, K.S., 1990. Axisymmetric creeping motion of drops through circular tubes. J. Fluid Mech. 210, 565–591.
Mortazavi, S., Tryggvasson, G., 2000. A numerical study of the motion of drops in Poiseuille flow. Part 1. Lateral migration of one drop. J. Fluid Mech. 411, 325–350.
Olbricht, W., Kung, D., 1992. The deformation & breakup of liquid drops in low Reynolds number flow through a capillary. Phys. Fluids A 4, 1347–1354.
Pozrikidis, C., 1992. Boundary Integral & Singularity Methods for Linearized Viscous Flow. Cambridge University Press, Cambridge, MA.
Rallison, J.M., Acrivos, A., 1978. A numerical study of the deformation and burst of a viscous drop in an extensional flow. J. Fluid Mech. 89, 191–200.
Rallison, J.M., 1981. A numerical study of the deformation & burst of a viscous drop in general shear flows. J. Fluid Mech. 109, 465–482.
Shapira, M., Haber, S., 1988. Low Reynolds number motion of a droplet between two parallel plates. Int. J. Multiphase Flow 14, 483–506.
Smart, J.R., Leighton, D.T., 1991. Measurement of the drift of a droplet due to the presence of a plane. Phys. Fluids A 3, 21–28.
Staben, M.E., Zinchenko, A.Z., Davis, R.H., 2003. Motion of a particle between two parallel plane walls in low-Reynolds number Poiseuille flow. Phys. Fluids 15, 1711–1733 (Erratum: Phys. Fluids 16, 4204).
Tsai, T., Miksis, M., 1994. Dynamics of a drop in a constricted capillary tube. J. Fluid Mech. 274, 197–217.
Uijttewaal, W.S.J., Nijihof, E.J., Heethaar, R.M., 1993. Droplet migration, deformation, and orientation in the presence of a plane wall: a numerical study compared with analytical theories. Phys. Fluids A 4, 819–825.
Zinchenko, A.Z., Rother, M.A., Davis, R.H., 1997. A novel boundary-integral algorithm for viscous interaction of deformable drops. Phys. Fluids 9, 1493–1511.
Zinchenko, A.Z., Rother, M.A., Davis, R.H., 1999. Cusping, capture, & breakup of interacting drops by a curvatureless boundary-integral algorithm. J. Fluid Mech. 391, 249–291.
Zinchenko, A.Z., Davis, R.H., 2000. An efficient algorithm for hydrodynamical interaction of many deformable drops. J. Comp. Phys. 157, 539–587.
Zinchenko, A.Z., Davis, R.H., 2005. A multipole-accelerated algorithm for close interaction of slightly deformable drops. J. Comp. Phys. 207, 695–735.